Resource

Cell

Absolute Quantification of Matrix Metabolites Reveals the Dynamics of Mitochondrial Metabolism

Graphical Abstract

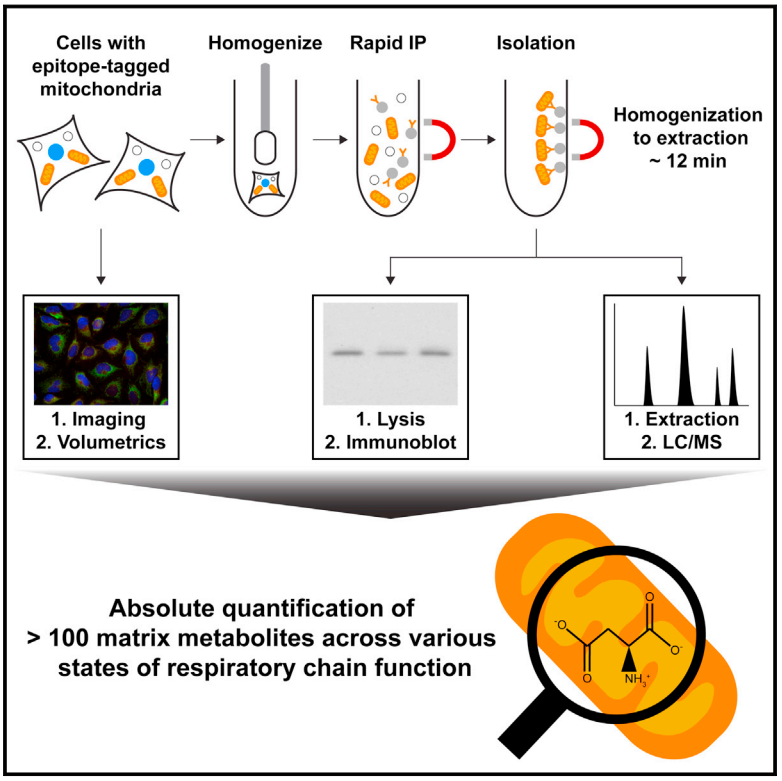

Authors

Walter W. Chen, Elizaveta Freinkman, Tim Wang, Kıvanç Birsoy, David M. Sabatini

Correspondence

sabatini@wi.mit.edu

In Brief

Metabolite profiling of intact mammalian mitochondria captures dynamics of mitochondrial metabolism not revealed by whole-cell analysis.

Highlights

- A workflow for absolute quantification of mitochondrial matrix metabolites
- Rapid and specific isolation of mitochondria from cells for metabolite profiling
- Profiling guided by MITObolome, a set of all predicted mitochondrial metabolites
- Dynamics of mitochondrial metabolism revealed by quantification of >100 metabolites

Chen et al., 2016, Cell *166*, 1324–1337
August 25, 2016
http://dx.doi.org/10.1016/j.cell.2016.07.040

CellPress

Cell

Resource

Absolute Quantification of Matrix Metabolites Reveals the Dynamics of Mitochondrial Metabolism

Walter W. Chen,[1,2,3,4] Elizaveta Freinkman,[1] Tim Wang,[1,2,3,4] Kıvanç Birsoy,[5] and David M. Sabatini[1,2,3,4,6,*]
[1]Whitehead Institute for Biomedical Research, Department of Biology, Massachusetts Institute of Technology, 9 Cambridge Center, Cambridge, MA 02142, USA
[2]Howard Hughes Medical Institute, Department of Biology, Massachusetts Institute of Technology, Cambridge, MA 02139, USA
[3]Koch Institute for Integrative Cancer Research, 77 Massachusetts Avenue, Cambridge, MA 02139, USA
[4]Broad Institute of Harvard and Massachusetts Institute of Technology, 7 Cambridge Center, Cambridge, MA 02142, USA
[5]Laboratory of Metabolic Regulation and Genetics, The Rockefeller University, New York City, NY 10065, USA
[6]Lead Contact
*Correspondence: sabatini@wi.mit.edu
http://dx.doi.org/10.1016/j.cell.2016.07.040

SUMMARY

Mitochondria house metabolic pathways that impact most aspects of cellular physiology. While metabolite profiling by mass spectrometry is widely applied at the whole-cell level, it is not routinely possible to measure the concentrations of small molecules in mammalian organelles. We describe a method for the rapid and specific isolation of mitochondria and use it in tandem with a database of predicted mitochondrial metabolites ("MITObolome") to measure the matrix concentrations of more than 100 metabolites across various states of respiratory chain (RC) function. Disruption of the RC reveals extensive compartmentalization of mitochondrial metabolism and signatures unique to the inhibition of each RC complex. Pyruvate enables the proliferation of RC-deficient cells but has surprisingly limited effects on matrix contents. Interestingly, despite failing to restore matrix NADH/NAD balance, pyruvate does increase aspartate, likely through the exchange of matrix glutamate for cytosolic aspartate. We demonstrate the value of mitochondrial metabolite profiling and describe a strategy applicable to other organelles.

INTRODUCTION

A hallmark of eukaryotic life is the membrane-bound organelles that compartmentalize specialized biochemical pathways within the cell. Enclosed by both outer and inner membranes, mitochondria carry out many essential metabolic processes, such as ATP generation by the respiratory chain (RC) (Wallace, 2013), aspartate synthesis by matrix aminotransferases (Birsoy et al., 2015; Cardaci et al., 2015; Safer, 1975; Sullivan et al., 2015), and long-chain fatty acid catabolism by the beta-oxidation pathway (Vianey-Liaud et al., 1987). Consistent with the critical role of mitochondria in maintaining cellular homeostasis, dysfunction of mitochondrial enzymes often leads to disease (Wallace, 2013).

Despite the importance of mitochondrial metabolism to cellular physiology, methods for systematically interrogating the polar metabolite contents of mitochondria in mammalian cells have been limited. In recent years, metabolite profiling of entire cells and tissues by mass spectrometry (MS) has greatly improved our understanding of metabolism by allowing for the simultaneous analysis of hundreds of metabolites from one sample. Such large-scale assessments have enabled the characterization of entire metabolic networks, which is often necessary to understand the effects of a perturbation on cellular metabolism (Cacciatore and Loda, 2015). Because mitochondria constitute a small fraction of cellular contents, whole-cell profiling is likely inadequate for monitoring changes within the mitochondrial matrix.

Several challenges hamper the application of metabolite profiling to subcellular organelles, such as mitochondria. Standard techniques for purifying mitochondria can take hours to complete, leading to a significant loss of metabolites because solute transporters and enzymes can have residual activity, even at low temperatures (Bowsher and Tobin, 2001; Matuszczyk et al., 2015; Ross-Inta et al., 2008). Commercially available kits for antibody-based isolation of mitochondria, such as the Miltenyi kits, are technically less cumbersome than other methods but utilize long immunopurification and wash steps. Abbreviated centrifugation protocols, selective membrane permeabilization, and non-aqueous fractionation all improve the speed of the workflow and have provided important insights into the metabolism of subcellular compartments, but the resultant mitochondrial preparations can be contaminated with cytosolic material, as well as other organelles, such as endoplasmic reticuli and lysosomes (Berry et al., 1991; Berthet and Baudhuin, 1967; Bestwick et al., 1982; Fly et al., 2015; Linskens et al., 2012; Matuszczyk et al., 2015; Roede et al., 2012; Tischler et al., 1977). Furthermore, the components of the traditional organellar isolation buffers (e.g., sucrose) can severely interfere with MS-based metabolite profiling (Roede et al., 2012). Thus, the interrogation of matrix metabolites in a straightforward, robust, and specific manner remains a significant challenge to the study of mitochondrial physiology.

To address this, we developed a new method that combines rapid immunocapture of epitope-tagged mitochondria with metabolite profiling by liquid chromatography and mass spectrometry (LC/MS). The isolation of mitochondria and extraction of their metabolites occurs within minutes of cellular homogenization and has greatly improved speed and specificity over prior approaches. Using this technique, we have generated a quantitative resource containing the matrix concentrations of more than 100 polar metabolites in cells under various states of RC function. This resource has enabled us to study the biology of pyruvate, which can reprogram cellular metabolism and mitigate the anti-proliferative effects of RC dysfunction in a manner poorly understood at the level of the mitochondrial matrix. Our work exemplifies the power of this quantitative resource for studying mitochondrial biology and provides a methodological framework for interrogating the metabolite contents of other subcellular compartments.

RESULTS AND DISCUSSION

A Method for the Rapid and Specific Isolation of Intact Mitochondria

To faithfully profile matrix metabolites, one needs a technique that is both rapid and capable of effectively separating mitochondria from other subcellular components. Existing methods do not adequately address both of these requirements. In addition, traditional mitochondrial isolation buffers contain high concentrations of solutes (e.g., sucrose) not suitable for LC/MS-based metabolomics because of the sensitivity of LC/MS instruments to small-molecule contaminants.

To isolate mitochondria rapidly and specifically, we developed an immunopurification (IP) strategy utilizing outer mitochondrial membrane proteins as handles for immunocapture, which enabled metabolite extraction from mitochondria in approximately 12 min following cellular homogenization. Instead of using an endogenous outer membrane protein, we chose an epitope-tagged recombinant protein as the IP handle because of the high sensitivity and specificity of various epitope-tags and their cognate antibodies. Three epitope tags were placed in tandem on the N terminus of EGFP fused to the well-characterized outer mitochondrial membrane localization sequence of OMP25 (Figure S1A) (Nemoto and De Camilli, 1999), and different tagging systems were tested for their ability to immunocapture mitochondria within 3.5 min. In HeLa cells, the epitope-tagged protein properly localized to mitochondria, as detected by the complete overlap of the EGFP signal with the established mitochondrial marker MitoTracker Deep Red FM (Figure 1A). Initial attempts to isolate mitochondria using a FLAG-based magnetic bead system commonly employed for protein IPs led to extremely poor yields (Figure S1B). As the FLAG epitope-antibody pairing has relatively high affinity, we suspected that the major issue was the nature of the beads rather than the epitope tag itself. FLAG antibody-conjugated beads are relatively large (~50 μm in diameter), but are made of a porous agarose matrix, which enables them to circumvent the reduced surface area associated with increased bead size. However, as the average diameter of the agarose pores and mitochondria are ~30 and ~500 nm, respectively, the majority of mitochondrial capture was probably limited to the surface of the beads, in which case reducing the bead size would lead to improved yields. Consistent with this, switching to a 3XHA-EGFP-OMP25 construct (HA-MITO) and the smaller cognate beads (non-porous, ~1 μm in diameter) led to dramatically improved yields in both protein (Figure S1B) and metabolite content (Figure S1C), while also preventing extra-mitochondrial metabolites from becoming trapped within the bead matrix.

In addition to the challenges of capturing mitochondria, the sensitivity of LC/MS instruments to small-molecule contaminants necessitated extensive optimization of isolation conditions. In initial experiments, we found that many components of traditional mitochondrial isolation buffers (e.g., sucrose, HEPES) significantly distorted LC/MS-based analyses, often leading to the complete loss of the signal for certain metabolites (Figure S1D). Prior work has demonstrated that KCl-based buffers can allow for the isolation of coupled mitochondria capable of supporting a membrane potential (Corcelli et al., 2010). As such, we developed an LC/MS-compatible buffer consisting only of KCl and KH_2PO_4 ("KPBS"), which had significantly improved performance (Figure S1E).

Utilizing our LC/MS-compatible isolation conditions and cells expressing 3XMyc-EGFP-OMP25 (Control-MITO) or HA-MITO, we developed a workflow for the quantitative interrogation of matrix metabolite concentrations (Figure 1B), the complete details of which are described in the STAR Methods. In brief, we quantified the moles of a matrix metabolite in the IP material by LC/MS-based metabolomics and the total matrix volume per cell by confocal microscopy. Immunoblot analyses of a mitochondrial marker in whole-cell lysates and the IP material gave the number of whole-cell equivalents present in the latter, which we combined with our microscopy-based measurements to determine the matrix volume of the isolated mitochondria. It is important to note that defining the true free space in the mitochondrial matrix is difficult because of its physical properties, and so we used the traditional estimate of matrix space determined by electron microscopy (Gerencser et al., 2012; Srere and Sumegi, 1986). Thus, by using both the moles of a metabolite and the associated matrix volume, we could derive a corresponding concentration.

Importantly, mitochondria isolated using our workflow exhibited good integrity and purity. Following isolation from cells incubated with MitoTracker Deep Red FM, mitochondria attached to beads still retained the dye, suggesting that the organelles were intact (Figure 1C). Immunoblot analyses of markers for mitochondria and other subcellular compartments revealed that our approach had significantly less contamination compared to differential centrifugation methods optimized for speed (Figure 1D) (Bestwick et al., 1982; Bogenhagen and Clayton, 1974). The residual LAMP2 signal in the IP material from both Control-MITO and HA-MITO cells likely reflects binding of free, non-lysosomal LAMP2 protein, and not binding of lysosomes, as we did not detect cathepsin C, a protein found in the lysosomal lumen, in the IP material (unpublished data) or cystine, a lysosomal metabolite, in isolated mitochondria (Table S1).

To quantitatively assess the integrity of purified mitochondria, we used a protein and metabolite marker to calculate how much of the mitochondrial material present in whole cells was captured

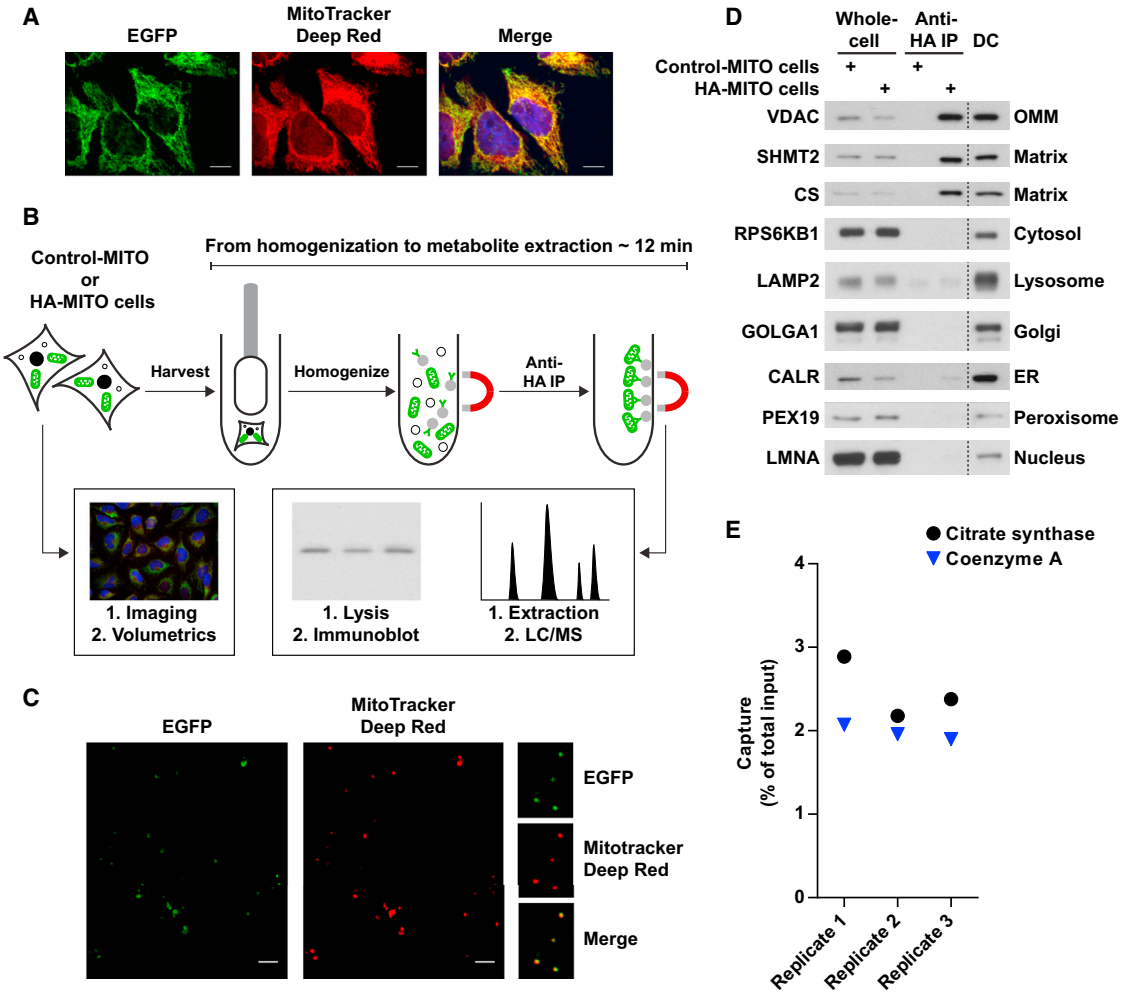

Figure 1. A Method for the Rapid and Specific Isolation of Intact Mitochondria

(A) The 3XTag-EGFP-OMP25 protein properly localizes to mitochondria. Representative confocal micrographs of HeLa cells expressing the recombinant EGFP-fusion protein (green). Mitochondria and nuclei were stained with MitoTracker Deep Red FM (red) and Hoechst (blue), respectively. Scale bars, 10 μm.

(B) Workflow for the absolute quantification of matrix metabolites. Cells expressing Control-MITO (Control-MITO cells) or HA-MITO (HA-MITO cells) are rapidly harvested and homogenized. HA-tagged mitochondria are isolated with a 3.5 min IP, washed, and then lysed for immunoblot analysis to determine the amount of captured mitochondria or extracted for LC/MS-based metabolomics to quantify metabolites. Confocal microscopy and volumetric analysis of the HA-MITO-expressing cells are used to determine total mitochondrial volume per cell, which is then adjusted based on the percentage of mitochondrial volume occupied by the matrix (~63.16% of mitochondrial volume = matrix) (Gerencser et al., 2012). All of these measurements are combined to calculate the matrix concentration of a metabolite.

(C) Epitope-tagged mitochondria isolated from cells incubated with MitoTracker Deep Red FM retain the dye. Representative confocal micrographs of beads with isolated mitochondria (green) and MitoTracker Deep Red FM signal (red). Right: magnifications of several beads with mitochondria. Scale bars, 5 μm.

(D) Purification of epitope-tagged mitochondria has significantly less contamination compared to a differential centrifugation method optimized for speed. Immunoblot analysis of whole-cell lysates (whole-cell) and lysates of mitochondria purified with anti-HA beads (anti-HA IP) or differential centrifugation (DC). Lysates were derived from cells expressing Control-MITO (Control-MITO cells) or HA-MITO (HA-MITO cells). The names of the protein markers used appear to the left of the blots, and their corresponding subcellular compartments appear to the right. OMM, outer mitochondrial membrane; matrix, mitochondrial matrix; Golgi, Golgi complex; ER, endoplasmic reticulum.

(E) Epitope-tagged mitochondria retain both soluble proteins and small molecules to similar degrees. A comparison of the amount of captured mitochondria as assessed by a matrix protein (citrate synthase) and a matrix metabolite (coenzyme A). Data are presented as a percentage of the total material present in harvested cells. Cells were cultured in DMEM without pyruvate.

See also Figure S1.

in each IP (i.e., yield) (Figure 1E). Both the enzyme citrate synthase (CS) and the metabolite coenzyme A (CoA) predominantly reside in the mitochondrial matrix, with only 10%–20% of cellular CoA being extra-mitochondrial (Idell-Wenger et al., 1978; Williamson and Corkey, 1979). Consistent with this, measurements of yield using either CS or CoA gave similar results, again demonstrating that the isolated mitochondria were intact, retaining both the protein and small-molecule markers to equal

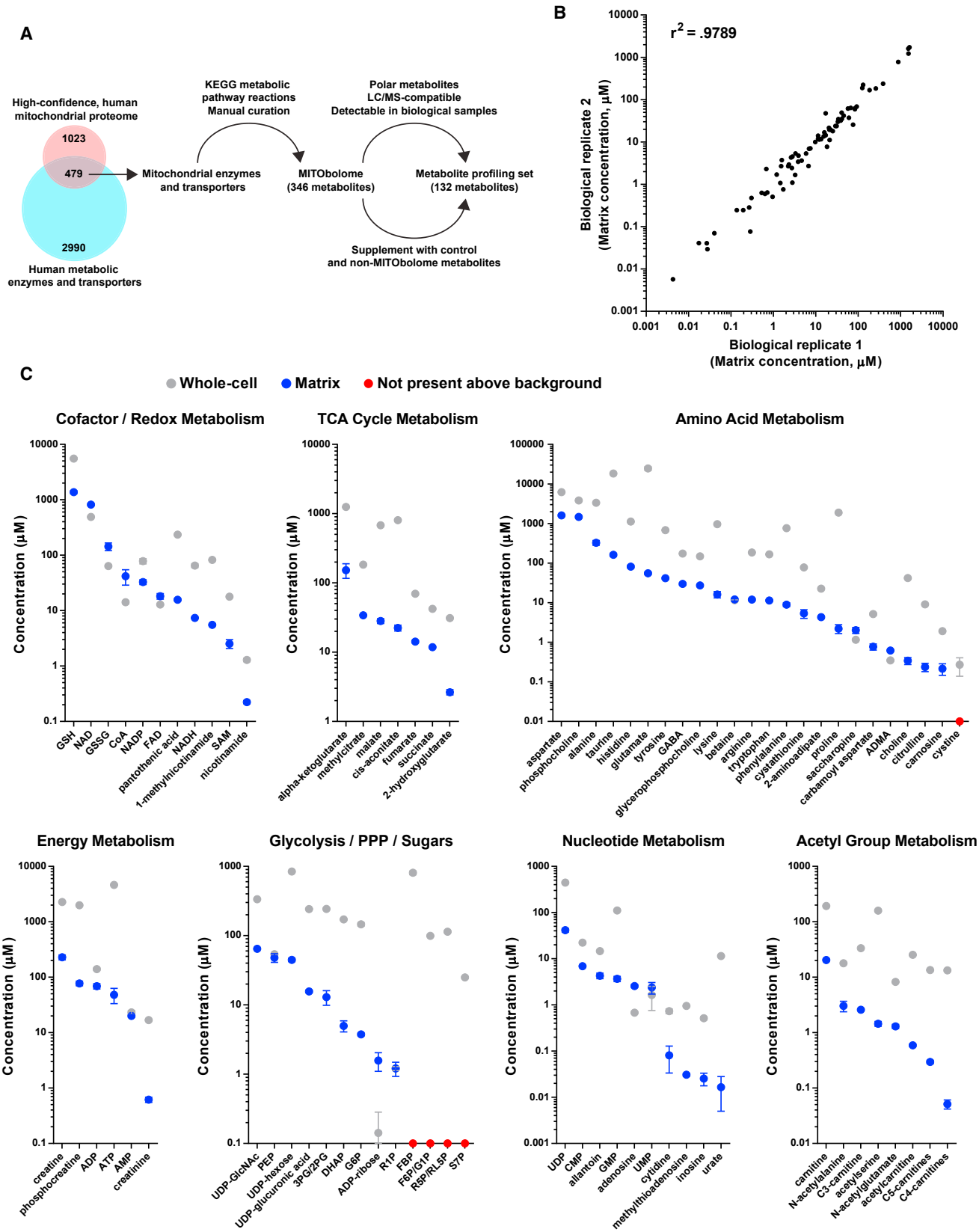

(legend on next page)

degrees (Figure 1E). The isolated mitochondria also retained a significant amount of the membrane-potential sensitive dye, TMRM, as well as its de-esterified intracellular form, TMR (Figure S1F). Importantly, treatment of cells with the uncoupler FCCP led to substantial loss of the dyes in mitochondria, demonstrating that the TMRM and TMR in isolated mitochondria were indeed membrane-potential responsive. Collectively, these data show that our method enables rapid and specific isolation of intact mitochondria for metabolite profiling.

Identities and Concentrations of Matrix Metabolites in Human Mitochondria

Because of the technical limitations of prior techniques, the identities and concentrations of polar, matrix metabolites in human mitochondria remain largely unknown. To address this, we began by generating a list of all predicted mitochondrial metabolites (the "MITObolome") by taking the known substrates, products, and cofactors of all mitochondrial enzymes and small-molecule transporters (Figure 2A). By using the MITObolome, we assembled a library of 132 chemical standards for the absolute quantification of metabolites within the mitochondrial matrix and whole cells (Figure 2A; Table S1). The STAR Methods describe in detail how the MITObolome and the final profiling set were assembled.

We quantified the concentrations of both whole-cell and mitochondrial samples using standard curves of every metabolite in the final profiling set (Table S1). Only total concentrations of metabolites were measured because distinguishing between free and bound populations remains a challenge in metabolomics. Reassuringly, comparisons of matrix concentrations of biological replicates demonstrated a high degree of correlation (Figure 2B). In addition, there was an excellent correlation between samples prepared by using the normal workflow and a workflow lengthened by 4 min, suggesting that there was not substantial distortion of the matrix metabolite profile in the time frame of our isolations, although it is difficult to know how mitochondria behave at time points earlier than our shortest isolations (Figure S2A). Various cofactors and redox pairs critical for mitochondrial reactions, such as NAD, NADH, FAD, NADP, GSH, GSSG, and SAM, were all found in mitochondria (Figure 2C). Metabolites involved in other mitochondrial processes, such as the TCA cycle, energy production, and fatty-acid metabolism, were present as well. Importantly, we did not observe signs of significant contamination from other subcellular compartments because various metabolites not expected to be abundant in mitochondria, such as cystine (lysosomes), sedoheptulose 7-phosphate, and fructose 1,6-bisphosphate (cytosol), were not present at levels above background. With regard to the accuracy of our measurements, our quantification of the matrix NADH/NAD ratio (0.009) agrees with prior studies that indirectly estimated matrix NADH/NAD ratios to span 0.006–0.125, depending on the cell type examined (Erecińska et al., 1978; Nishiki et al., 1978). Taken together, these data indicate that our LC/MS-based workflow can be used to quantitatively study the metabolic landscape of the mitochondrial matrix.

Concentrations of most metabolites within the mitochondrial matrix were generally lower than the corresponding measurements made at the whole-cell level (Figures 2C and S2B). The most abundant metabolites were aspartate (1.6 mM), phosphocholine (1.47 mM), GSH (1.37 mM), and NAD (818 μM), each of which participate in distinct metabolic processes (Figure 2C). In contrast, the least abundant were methylthioadenosine (31 nM), inosine (26 nM), and urate (17 nM), all metabolites involved in nucleotide metabolism. As a whole, matrix concentrations spanned a wide range of values, even within the same family of metabolites, underscoring the diversity of the metabolic space within mitochondria.

One particularly diverse class of matrix metabolites is amino acids, which participate in both metabolic reactions and the synthesis of the 13 mitochondrially encoded proteins required for RC activity (Elo et al., 2012). The majority of proteinogenic amino acids were found in mitochondria (Figure 2C; Tables S1, S2, and S3), with the most abundant being aspartate (1.6 mM), alanine (327 μM), and histidine (82 μM) (Figure 2C). Although the mitochondrial abundance of different amino acids will likely vary among different cell types, the high concentration of aspartate agrees with recent findings demonstrating that a critical role for mitochondria in supporting cell proliferation is aspartate synthesis (Birsoy et al., 2015; Sullivan et al., 2015).

We also examined the relationships between the $K_M^{\text{Amino acid}}$ values of different mitochondrial aminoacyl-tRNA synthetases and the concentrations of their cognate amino acids. For example, the K_M^{Asp} of human mitochondrial aspartyl-tRNA synthetase is 1.5 μM (Messmer et al., 2009), while the average baseline matrix concentration of aspartate across all experiments was 1.11 mM (Tables S1, S2, and S3). In the case of aspartate, the matrix concentration is maintained well above the K_M^{Asp} of the aspartyl-tRNA synthetase, likely ensuring that fluctuations in the abundance of aspartate do not affect charging of the cognate tRNAs. Yet one interesting instance in which this was not the case is phenylalanine. The average baseline matrix concentration of phenylalanine across all experiments was 24.2 μM (Tables S1, S2, and S3). However, the K_M^{Phe} of the mitochondrial phenylalanyl-tRNA synthetase (FARS2) is 7.3 μM. Mutations in

Figure 2. Identities and Concentrations of Matrix Metabolites in Human Mitochondria

(A) Generation of the MITObolome and the set of 132 metabolites for which concentrations were measured. Mitochondrial proteomic data were cross-referenced with a list of all human metabolic enzymes and transporters. The overlap between these two datasets was used in conjunction with KEGG and manual curation to assemble the MITObolome, a list of all predicted mitochondrial metabolites. The MITObolome was filtered on the indicated criteria and supplemented with additional metabolites to generate the final set of 132 metabolites for which concentrations were measured. KEGG, Kyoto Encyclopedia of Genes and Genomes.

(B) Absolute quantification of matrix metabolites is highly consistent between experiments. Matrix concentrations of metabolites from two biological replicates were compared, and a Pearson correlation coefficient was calculated.

(C) Concentrations of metabolites in the mitochondrial matrix and in whole cells. Data are from cells cultured in DME base media (mean ± SEM, n = 3). For each group, metabolites are arranged from most abundant to least abundant within mitochondria. Metabolites not considered to be present at levels above background are plotted as red dots on the x axis. See Table S1 for the full names of certain abbreviated metabolites. PPP, pentose phosphate pathway.

See also Figure S2 and Table S1.

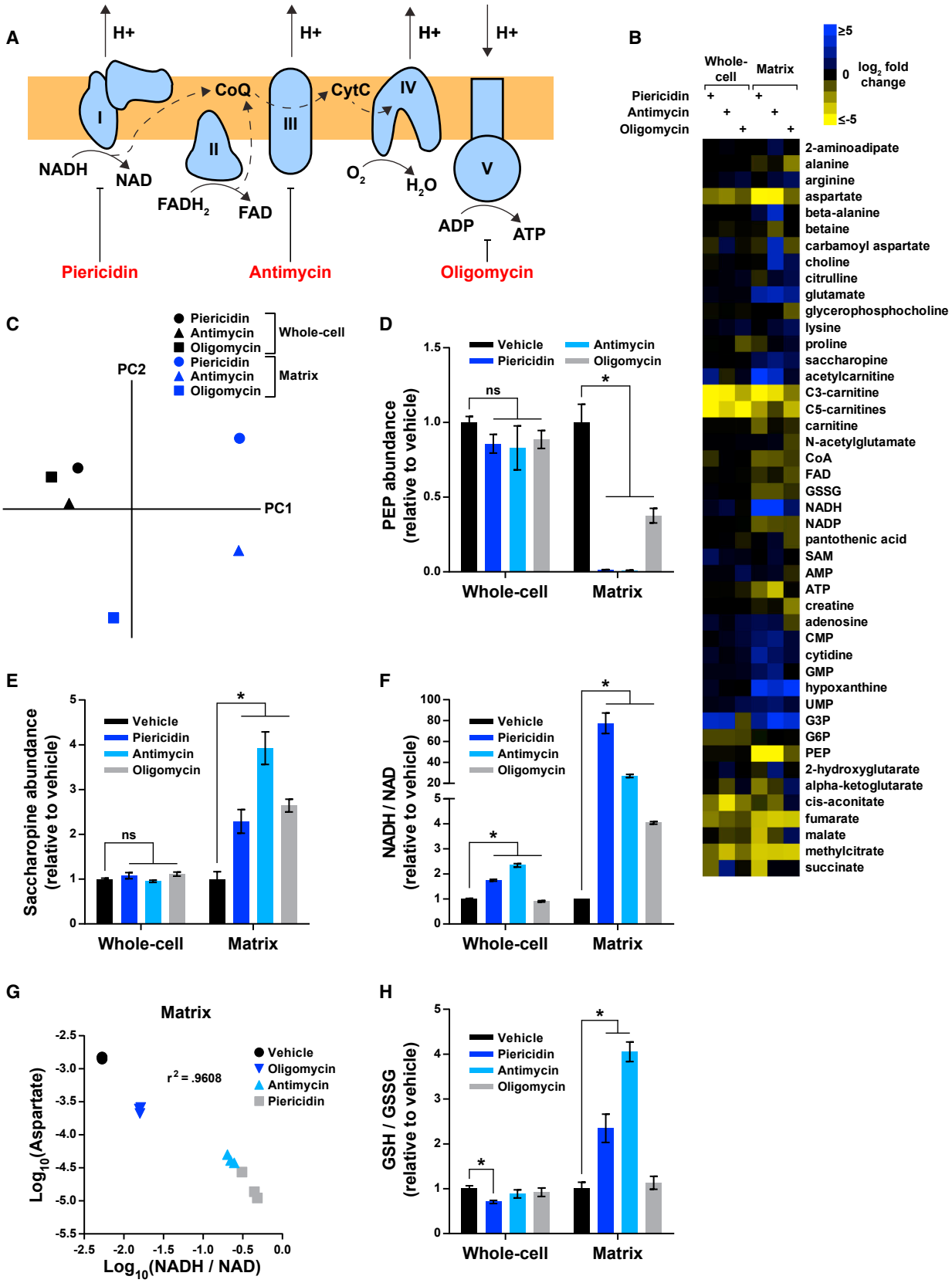

(legend on next page)

FARS2 can reduce levels of mitochondrially encoded proteins and cause fatal epileptic mitochondrial encephalopathy by decreasing the affinity of the FARS2 enzyme for its various substrates (i.e., ATP, tRNA, phenylalanine). In contrast to other pathogenic mutations, a D391V substitution in FARS2 does not substantially alter K_M^{ATP} and K_M^{tRNA}, but increases the K_M^{Phe} of FARS2 from 7.3 to 20.9 μM (Elo et al., 2012). Based on our measurements of matrix phenylalanine concentrations, this could lead to inefficient charging of mitochondrial $tRNA^{Phe}$ and reduced mitochondrial protein synthesis. These findings thus provide additional insight into the pathogenic basis of the D391V form of FARS2 and exemplify how our quantitative profile of mitochondria can be used with in vitro characterizations of mitochondrial proteins.

To complement our MITObolome-based approach of profiling mitochondria, we also performed highly targeted and untargeted LC/MS-based metabolomics. By using a tSIM (targeted selected ion monitoring) scan, we quantified additional nucleotide species in mitochondria that were difficult to detect using a standard full scan (Table S1). In addition, using untargeted metabolomics, we uncovered numerous molecules not predicted to be mitochondrial based on the MITObolome (Table S1). As untargeted metabolomics does not provide definitive metabolite identification, validation of peaks is critical for proper data analysis. By matching the characteristics of the peak from our untargeted analysis with those of the corresponding chemical standard, we identified ADP-ribose as a metabolite not previously assigned to the mitochondria based on the databases we have examined (Table S1). ADP-ribose is a substrate for poly(ADP-ribosylating) enzymes, which localize to mitochondria and may maintain the integrity of mitochondrial DNA (Scovassi, 2004). Taken together, these results demonstrate the utility of our targeted and untargeted approaches for studying the metabolite contents of mitochondria.

Whole-Cell Analyses Do Not Capture the Dynamics of Mitochondrial Metabolism

Comprised of complexes I–V, the RC oxidizes NADH and $FADH_2$ to generate a proton gradient that drives the rotation of complex V and the synthesis of ATP (Figure 3A). Inherited defects in RC complexes cause various forms of mitochondrial disease (Wallace, 2013). However, our understanding of the metabolic consequences of RC pathology is incomplete, especially at the mitochondrial level.

To model different disease states, we treated cells with penetrant doses of piericidin (complex I inhibitor), antimycin (complex III inhibitor), and oligomycin (complex V inhibitor) (Figure 3A; Table S2). While the whole-cell responses to these inhibitors have been previously studied (Birsoy et al., 2015; Chen et al., 2014; Mullen et al., 2012; Shaham et al., 2010; Sullivan et al., 2015), the alterations in matrix metabolites have not. Because of the compartmentalized nature of mitochondria, matrix metabolites can be regulated in unique ways and be present at levels much lower than those in other subcellular compartments. For these reasons, we hypothesized that whole-cell studies do not accurately capture the dynamics of matrix metabolites during RC dysfunction.

In cells treated with each of the three inhibitors, the metabolite profiles of whole cells and the mitochondrial matrix were highly different (Figures 3B and 3C). For some metabolites, such as aspartate, we observed similar trends in both, but the extent of the change was generally greater in the matrix (Figure 3B). For other metabolites, such as phosphoenolpyruvate (PEP) and saccharopine, the differences between whole cells and the matrix were dramatic (Figures 3D and 3E). In these cases, direct interrogation of mitochondria uncovered alterations in critical metabolic processes that would have gone undetected using whole-cell metabolomics.

Two distinct pathways, glycolysis and gluconeogenesis, generate PEP in mammalian cells. Enolase catalyzes the formation of PEP from 2-phosphoglycerate in the cytosol, and PEP carboxykinase (PCK) generates PEP from oxaloacetate in the matrix and cytosol. The mitochondrial PCK (PCK2) reaction is a rate-limiting step in the gluconeogenic pathway. However, it has been difficult to study PCK2 because of the substantial contribution of cytosolic pools of PEP to the whole-cell signal (Stark et al., 2014). Matrix PEP levels significantly dropped across all three forms of RC dysfunction, with the severity of the phenotype correlating well with the relative change in matrix aspartate, a proxy for the PCK2 substrate, oxaloacetate (Ke

Figure 3. Compartmentalized Dynamics of Matrix Metabolites during RC Dysfunction

(A) Schematic depicting the function of each RC component and the corresponding sites of inhibition for piericidin, antimycin, and oligomycin. Complexes I–IV transfer high-energy reducing equivalents from NADH and $FADH_2$ to O_2, generating a proton gradient in the process. Complex V utilizes this gradient to synthesize ATP. CoQ, coenzyme Q; CytC, cytochrome C.

(B) Heat map representing changes in metabolite concentrations following inhibition of complex I, III, or V, as assessed by whole-cell and mitochondrial metabolomics. For each metabolite and inhibitor, the mean log_2-transformed fold change is relative to the corresponding whole-cell or matrix concentration of vehicle-treated cells (n = 3). To be included in the heat map, metabolites had to change at least 2-fold following inhibition of an RC complex. See Table S2 for the detailed criteria used to generate this heat map and for the concentrations of all metabolites.

(C) Whole-cell and matrix profiles during RC dysfunction are substantially different. Principal component analysis of metabolite changes in Figure 3B as assessed by profiling of the mitochondrial matrix (blue) or of whole cells (black).

(D) RC inhibition lowers matrix PEP.

(E) RC inhibition increases matrix saccharopine.

(F) The NADH/NAD imbalance during RC dysfunction is more pronounced in the matrix than on the whole-cell level.

(G) The relationship between matrix aspartate and the matrix NADH/NAD ratio can be modeled as a power function. Log_{10}-transformed values of matrix aspartate concentrations (units of M) and NADH/NAD ratios were compared across different states of RC function, and a Pearson correlation coefficient was calculated.

(H) Inhibition of complexes I and III increases matrix GSH/GSSG ratios. For all panels, unless indicated otherwise, all experiments were performed in DMEM without pyruvate and all measurements are normalized to the corresponding whole-cell or matrix concentrations of vehicle-treated cells (mean ± SEM, n = 3, $^*p < 0.05$).

See also Table S2.

et al., 2015) (Figures 3B and 3D). Underscoring the importance of directly profiling mitochondria, whole-cell PEP levels did not significantly change during inhibition of the RC (Figure 3D). Collectively, these data demonstrate that RC dysfunction leads to reduced oxaloacetate, a TCA cycle metabolite, and consequently a dramatic impairment of PCK2 activity, an important step in gluconeogenesis. These findings are in line with prior work arguing that PCK2 also links TCA cycle activity to gluconeogenesis through the enzyme's dependence on GTP, which is formed by the TCA cycle enzyme, succinyl-CoA synthetase (Stark et al., 2009).

A similarly compartmentalized defect occurred in the lysine degradation pathway during all forms of RC dysfunction, as evidenced by the accumulation of matrix saccharopine (Figure 3E). The matrix enzyme, aminoadipate-semialdehyde synthase (AASS) metabolizes saccharopine, a breakdown product of lysine, in an NAD-dependent manner (Markovitz et al., 1984). Accumulation of NADH within the matrix likely leads to inhibition of AASS activity during RC dysfunction (Figure 3B). Similar to PEP, saccharopine did not significantly change on the whole-cell level, likely due to the cytosolic pool of saccharopine being larger than the matrix pool (Figure 3E). However, in contrast to the production of PEP in multiple subcellular compartments, only mitochondria generate saccharopine (Kanehisa and Goto, 2000). Thus, whole-cell studies can fail to detect a change in matrix metabolism even when the participating metabolite has a purely mitochondrial origin. Taken together, these data demonstrate substantial compartmentalization of metabolic changes during RC dysfunction that necessitates profiling at the matrix level.

Extensive Compartmentalization of Core Redox and Antioxidant Metabolism in Cells with RC Inhibition

Redox balance and antioxidant defense are two core mitochondrial processes critical for maintaining matrix homeostasis and regulated by the ratios of NADH/NAD and GSH/GSSG, respectively (Wheaton et al., 2014). We were particularly interested in the behavior of these processes as it has been speculated that during RC dysfunction the mitochondrial changes in NADH/NAD and GSH/GSSG are likely distinct from those seen in whole cells (Van Vranken and Rutter, 2015; Wheaton et al., 2014). Consistent with this, there were dramatic differences in the degree of NADH/NAD imbalance in whole cells and the mitochondrial matrix during RC dysfunction (Figure 3F). Whole-cell NADH/NAD ratios increased during RC dysfunction by a maximum of 2.3-fold following complex III inhibition and did not increase at all during complex V inhibition. In contrast, all three inhibitors significantly elevated matrix NADH/NAD ratios, with complex I inhibition increasing the NADH/NAD ratio ~77-fold. The smaller changes in whole-cell NADH/NAD ratios during RC blockade are consistent with matrix NADH being a small portion of the whole-cell pool (Table S2). In addition, while RC dysfunction largely cripples the mitochondrial axis of NAD regeneration, lactate dehydrogenase can still replenish cytosolic NAD, thereby mitigating cytosolic NADH/NAD imbalance.

A major consequence of RC dysfunction is a decreased level of aspartate, which mitochondria produce primarily through a series of NAD-dependent reactions (Birsoy et al., 2015; Safer, 1975; Sullivan et al., 2015). As such, we hypothesized that there should be a relationship between matrix NADH/NAD ratios and aspartate concentrations across different states of RC function. Indeed, there was an excellent correlation between the $\log_{10}$-transformed values of matrix aspartate and NADH/NAD, which demonstrates that the relationship between aspartate and the NADH/NAD ratio can be modeled as a power function (Figure 3G). Consistent with this, even a relatively mild increase in the NADH/NAD ratio (i.e., oligomycin treatment) could account for the majority of the loss in matrix aspartate, suggesting that aspartate synthesis is quite sensitive to changes in matrix NADH/NAD redox balance.

In addition to NAD and NADH, we also examined the behavior of GSH and GSSG, another redox pair critical for mitochondrial function and one often used as a metric for oxidative stress. In contrast to whole cells, inhibition of either complex I or III significantly increased the matrix GSH/GSSG ratio (Figure 3H), demonstrating that disruption of RC function can lead to a state in which there is less oxidative stress in the matrix. These data agree with models in which RC activity generates a significant amount of reactive oxygen species in mitochondria (Wheaton et al., 2014), but may also reflect a relationship between NADH/NAD and GSH/GSSG ratios that is mediated through mitochondrial transhydrogenases, which can utilize NADH to generate NADPH, a redox molecule critical for driving GSH formation (Mullen et al., 2012). Collectively, these results reveal how profiling the metabolite contents of mitochondria can even uncover new information about well-studied core processes, such as redox balance and antioxidant defense.

MITObolomics Reveals Unique Signatures of Complex I, III, and V Inhibition

Complexes I, III, and V have non-redundant functions in the RC, and defects in each can lead to distinct forms of mitochondrial disease (Wallace, 2013). While general features of RC dysfunction, such as NADH/NAD imbalance, are well appreciated, our understanding of the metabolic consequences of inhibiting specific RC complexes remains incomplete, particularly at the mitochondrial level. To that end, we identified metabolic alterations in the matrix unique to the inhibition of complex I, III, or V.

A striking example of such a metabolic signature is the accumulation of acetyl-CoA in the matrix of cells with complex I inhibition, which we did not observe in any other form of RC dysfunction (Figure 4A). Whole-cell acetyl-CoA did not recapitulate the changes in matrix acetyl-CoA, likely due to the larger extra-mitochondrial pools of acetyl-CoA. Acetyl-CoA normally enters the TCA cycle through the action of citrate synthase, an enzyme that decreases in activity when the NADH/NAD ratio is high. Although the reason that complex V blockade does not lead to acetyl-CoA accumulation is likely the smaller degree of NADH/NAD imbalance, the same cannot be said for complex III inhibition, which increased the matrix NADH/NAD ratio substantially (Figure 3F). Consistent with complexes I and III altering the matrix NADH/NAD ratio to a comparable degree, both forms of RC dysfunction reduced matrix aspartate to a similar extent (Figure 3G). However, one of the distinguishing features of complex III blockade is that it also impairs the regeneration of FAD. The first step of fatty acid oxidation, which significantly

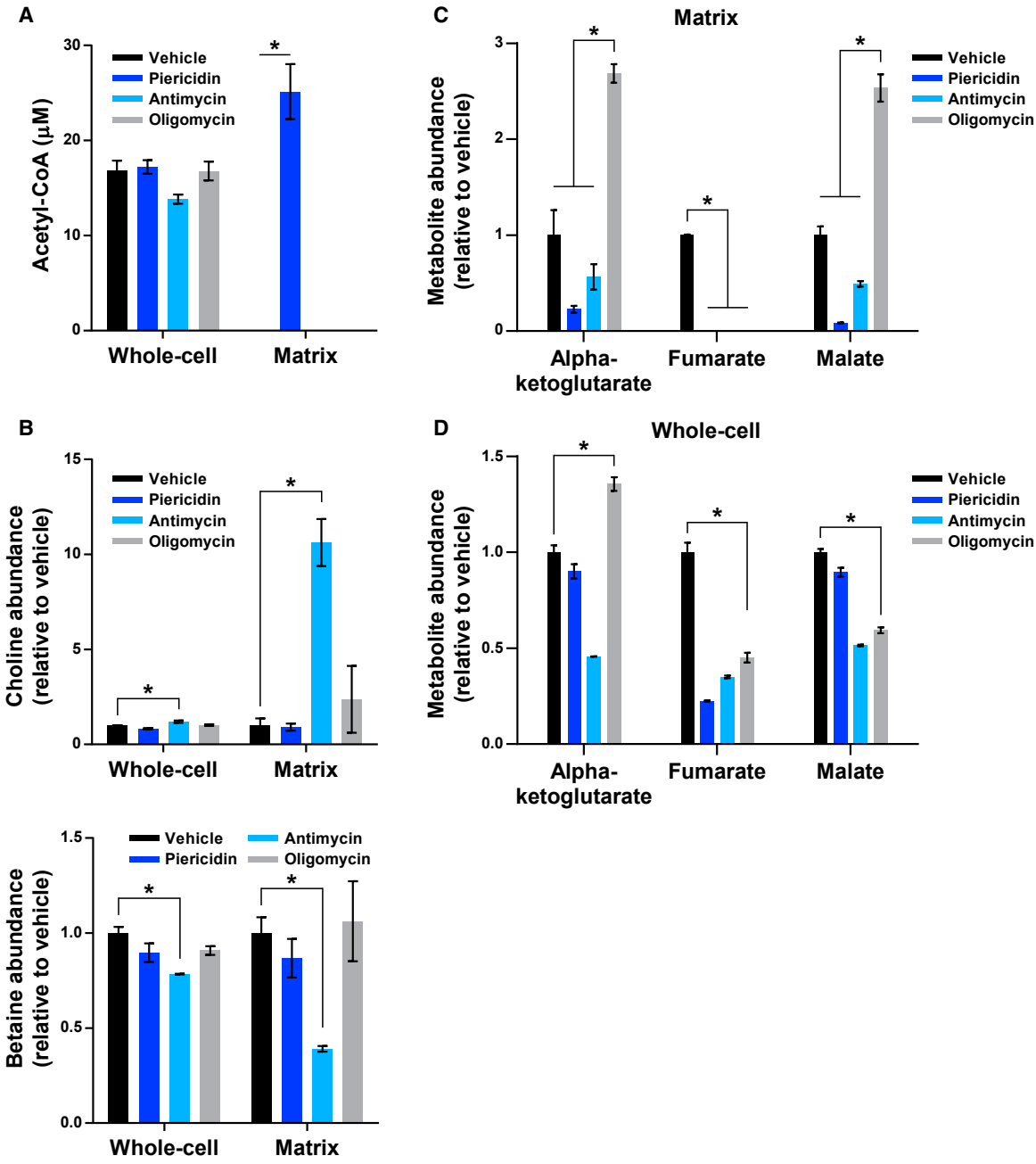

Figure 4. Hallmarks of Matrix Metabolism under Different Forms of RC Inhibition

(A) Matrix acetyl-CoA only accumulates during complex I inhibition. Data are presented as whole-cell or matrix concentrations that have not been normalized.

(B) Complex III dysfunction inhibits the transformation of choline to betaine in the matrix.

(C) Complex V inhibition leads to the accumulation of matrix metabolites at opposite ends of the TCA cycle.

(D) The pattern of changes seen in matrix TCA cycle metabolites during complex V inhibition is not recapitulated at the whole-cell level. For all panels, unless indicated otherwise, all experiments were performed in DMEM without pyruvate, and all measurements are normalized to the corresponding whole-cell or matrix concentrations of vehicle-treated cells (mean ± SEM, n = 3, *p < 0.05).

See also Figure S3 and Table S2.

contributes to matrix acetyl-CoA pools, requires FAD (Vianey-Liaud et al., 1987). As such, acetyl-CoA likely does not accumulate following complex III inhibition because it cannot be generated in sufficient amounts. While fatty acid oxidation also requires NAD to generate acetyl-CoA (Vianey-Liaud et al., 1987), it is possible that residual flux through the

NAD-dependent step during complex I inhibition can still lead to acetyl-CoA accumulation. There is precedent for this as succinate accumulates during complex III inhibition despite reduced activity of the upstream enzyme, alpha-ketoglutarate dehydrogenase (Mullen et al., 2012). Interestingly, prior work has shown that excess acetyl-CoA can lead to non-enzymatic acetylation of mitochondrial proteins, a pathological process countered by the mitochondrial deacetylase, SIRT3 (Wagner and Payne, 2013). Our findings thus suggest that complex I inhibition may impose a greater burden on the SIRT3 system than do other forms of RC dysfunction.

It is well appreciated that complex III inhibition leads to the accumulation of succinate in cells (Mullen et al., 2012). Interestingly, while succinate behaved as expected at the whole-cell level, it did not appreciably accumulate in the matrix, suggesting that excess succinate is rapidly exported into the cytosol (Figure 3B). We did, however, observe a substantial accumulation of choline and loss of betaine in the mitochondrial matrix, which was unique to complex III inhibition (Figure 4B). Similar trends were observed in whole cells, although at much lesser degrees. This pattern of metabolic changes likely reflects a decrease in the activity of choline dehydrogenase, a matrix enzyme dependent on FAD. These data demonstrate that only complex III inhibition decreases mitochondrial synthesis of betaine, which can play an important role in the cellular maintenance of the SAM-SAH cycle of methylation (Kanehisa and Goto, 2000).

Inhibition of complex V led to mitochondrial abnormalities also seen with inhibition of complexes I and III (e.g., loss of matrix aspartate) but generated a distinctive distribution of TCA cycle metabolites within the matrix that was not seen on the whole-cell level (Figures 4C and 4D). Indeed, matrix metabolites on opposite ends of the cycle accumulated (i.e., alpha-ketoglutarate, malate) and decreased dramatically (i.e., fumarate). This is in contrast to inhibition of complexes I and III, which caused a general decrease of TCA cycle components from alpha-ketoglutarate onward (Figures 3B and 4C), and suggests greater oxidative TCA cycle activity during complex V inhibition.

Although we have highlighted a few notable examples to exemplify the utility of our approach, many other interesting phenomena were specific to certain forms of RC dysfunction. For example, complex I inhibition led to a massive increase in the matrix acetylcarnitine/carnitine ratio (>250-fold), compared to the other forms of RC blockade (<20-fold), whereas only complex III inhibition significantly increased levels of carbamoyl aspartate (Figures S3A and S3B). Future work would be needed to fully appreciate the impacts of these metabolic changes during RC pathology. More generally though, these studies reveal that specific states of RC dysfunction lead to unique alterations in matrix metabolites.

Amelioration of RC Dysfunction with Pyruvate Increases Matrix Aspartate without Restoration of the Matrix NADH/NAD Ratio

Pyruvate has been known for decades to suppress the anti-proliferative effects of RC dysfunction (Harris, 1980; King and Attardi, 1989). Recent work shows that pyruvate supplementation during RC dysfunction leads to regeneration of NAD and induction of aspartate synthesis in the cytosol (Birsoy et al., 2015; Sullivan et al., 2015). Given the ability of pyruvate to substantially alter cytosolic metabolism, we asked whether it could similarly reverse the mitochondrial defects associated with RC dysfunction.

Inhibition of complex I, III, or V has been shown to reduce aspartate at the whole-cell level (Birsoy et al., 2015; Sullivan et al., 2015). To improve our chances of seeing pyruvate-mediated rescue during the time frame of our treatment conditions, we examined complex V blockade with oligomycin, which causes significant, but relatively modest, NADH/NAD imbalance in the mitochondrial matrix (Figure 3F). Inhibition of complex V did not increase the whole-cell NADH/NAD ratio, but pyruvate did lower NADH/NAD ratios, regardless of treatment conditions, demonstrating that pyruvate was driving NAD regeneration (Figure S4). Consistent with this, pyruvate supplementation significantly rescued whole-cell aspartate during complex V inhibition, but also led to a significant improvement in matrix aspartate as well (Figure 5A).

Interestingly, despite the ability of pyruvate to increase NAD regeneration in the cytosol, the matrix NADH/NAD ratio did not improve with pyruvate supplementation during complex V inhibition (Figure 5B). In contrast to the relationship between matrix NADH/NAD ratios and aspartate in the absence of pyruvate (Figure 3G), this was a unique example in which the behavior of aspartate did not correlate well with changes in NADH/NAD balance (Figures 5A and 5B). Thus, pyruvate can increase matrix aspartate without ameliorating the NADH/NAD imbalance caused by RC dysfunction.

Consistent with its inability to correct the matrix NADH/NAD ratio, pyruvate did not significantly alter the behavior of metabolites that were substantially changed during oligomycin treatment (Figure 5C; Table S3). Indeed, there were good correlations between the metabolic profiles of cells treated with oligomycin in the presence and absence of pyruvate at the matrix level, as well as the whole-cell level (Figure 5D).

Interestingly, pyruvate supplementation led to reduced glutamate accumulation during complex V blockade (Table S3). Matrix glutamate accumulated in all forms of RC dysfunction tested (Figure 3B), likely due to inhibition of the NAD-dependent mitochondrial glutamate dehydrogenases. However, because pyruvate did not restore the matrix NADH/NAD ratio (Figure 5B), it is unlikely that redox changes reduced the accumulation of glutamate. Taking advantage of our absolute quantification of metabolites, we compared the matrix levels of glutamate and aspartate. Interestingly, following pyruvate supplementation, the decrease in the concentration of matrix glutamate was very similar in magnitude to the increase in the concentration of matrix aspartate (Figure 5E; Table S3; see the STAR Methods for calculations). These findings are consistent with the behavior of mitochondrial aspartate-glutamate transporters, which exchange aspartate for glutamate (Palmieri, 2013). During RC inhibition in the presence of pyruvate, the accumulation of cytosolic aspartate and matrix glutamate could potentially drive the antiport activity of these transporters. We thus suggest that pyruvate improves cytosolic and matrix aspartate through two distinct metabolic routes, with the mitochondrial axis not

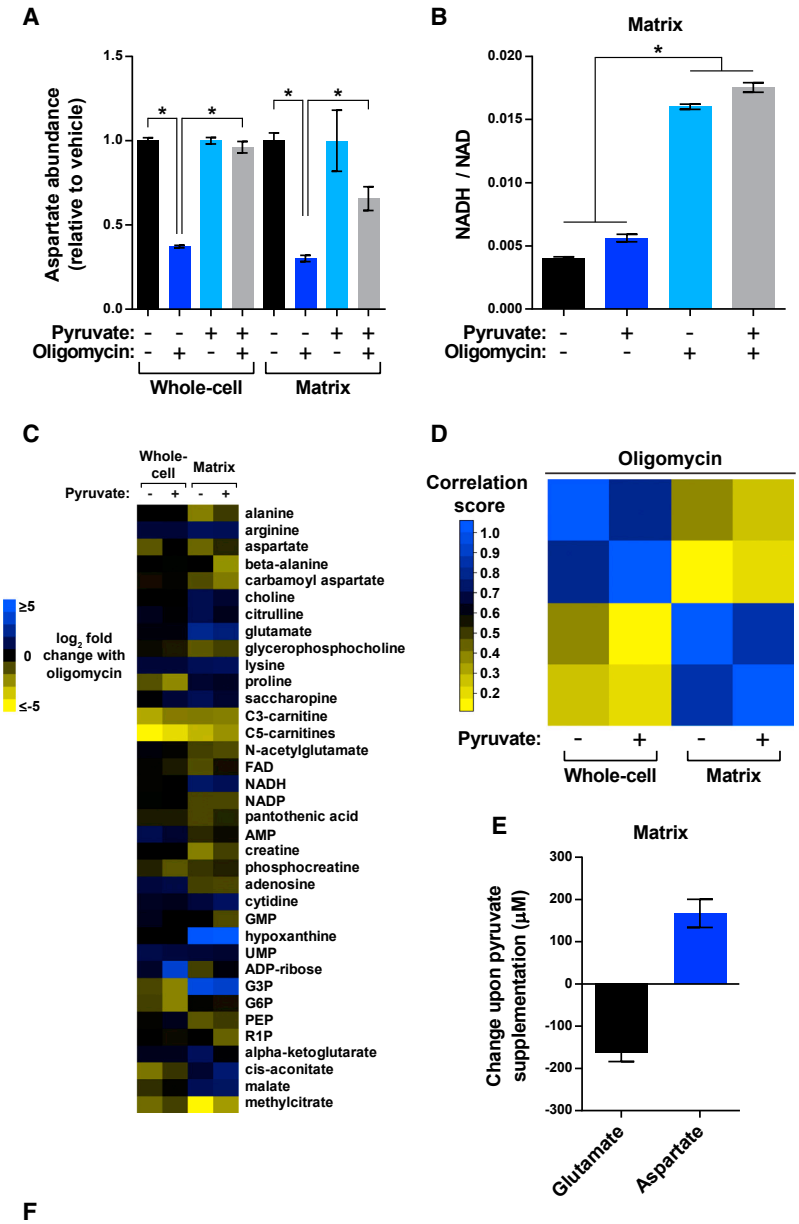

Figure 5. Amelioration of RC Dysfunction with Pyruvate Increases Matrix Aspartate without Restoration of the Matrix NADH/NAD Ratio

(A) Pyruvate can ameliorate loss of aspartate during complex V blockade, both in whole cells and the mitochondrial matrix. All measurements are normalized to the corresponding whole-cell or matrix concentrations of vehicle-treated cells.

(B) Pyruvate does not ameliorate matrix NADH/NAD imbalance during complex V dysfunction. Data are presented as NADH/NAD ratios that have not been normalized.

(C) Heat map representing changes in metabolite concentrations following inhibition of complex V in the presence and in the absence of pyruvate, as assessed by whole-cell and mitochondrial metabolomics. For each metabolite, the mean $\log_2$-transformed fold change is relative to the corresponding whole-cell or matrix concentration of vehicle-treated cells in the absence or in the presence of pyruvate (n = 3). To be included in the heat map, metabolites had to change at least 2-fold following inhibition of complex V. See Table S3 for the detailed criteria used to generate this heat map and for the concentrations of all metabolites.

(D) Pyruvate supplementation has limited effects on the metabolite contents of whole cells and the mitochondrial matrix during complex V blockade. A Pearson correlation analysis of the metabolic changes depicted in Figure 5C.

(E) During complex V inhibition, pyruvate supplementation leads to a reduction in matrix glutamate similar in magnitude to the increase in matrix aspartate. Data are presented as matrix concentrations that have not been normalized. See the STAR Methods for the details of these calculations. For all panels, unless indicated otherwise, experiments were performed in DMEM with and without pyruvate (1 mM), and all measurements are normalized to the corresponding whole-cell or matrix concentrations of vehicle-treated cells (mean ± SEM, n = 3, *$p < 0.05$).

(F) Model illustrating the effects of pyruvate on cytosolic and matrix aspartate during RC dysfunction.

See also Figure S4 and Table S3.

even dependent on restoration of the matrix NADH/NAD ratio (Figure 5F).

Conclusions

The speed and specificity of existing isolation protocols have made it challenging to profile the polar metabolite contents of mitochondria in mammalian systems. To address this, we have developed a new technique that combines high-affinity capture of epitope-tagged mitochondria and LC/MS-based metabolomics. This has allowed us to generate a quantitative resource containing matrix concentrations of more than 100 metabolites under different states of RC function, revealing the compartmentalized dynamics of numerous metabolic processes. From this work, we have found that pyruvate has limited effects on matrix metabolites during RC pathology, but can increase matrix aspartate without ameliorating matrix NADH/NAD imbalance.

Increasing matrix aspartate is important during RC pathology because mitochondria require aspartate to synthesize critical RC components. In states of partial RC dysfunction (e.g., complex I inhibition), residual RC activity preserves key cellular processes, such as de novo pyrimidine synthesis (King and Attardi, 1989) and mitochondrial membrane potential (Birsoy et al., 2015; Chen et al., 2014). Thus, if pyruvate solely increased aspartate in the cytosolic compartment of cells with partial RC dysfunction, then it is possible that the existing deficiency in matrix aspartate could lead to decreased mitochondrial protein synthesis and further cellular pathology.

Taken together, we believe that this work demonstrates the power of our methodology for studying mitochondrial metabolism. The use of epitope tags to isolate mitochondria allows for spatiotemporal control over which cell type one purifies from, a particularly useful feature for in vivo metabolic studies. More generally, the relative ease of designing epitope-tagged handles for different organelles suggests that our strategy can be extended to other subcellular compartments, thus allowing for in-depth characterization of organellar metabolites in mammalian systems.

STAR★METHODS

Detailed methods are provided in the online version of this paper and include the following:

- KEY RESOURCES TABLE
- CONTACT FOR REAGENT AND RESOURCE SHARING
- EXPERIMENTAL MODEL AND SUBJECT DETAILS
  - Generation of Cells with Epitope-Tagged Mitochondria
  - Cell Culture Conditions
- METHOD DETAILS
  - Magnetic Beads, Antibodies, Reagents, and Constructs
  - Immunoblotting
  - Confocal Microscopy
  - MITObolome and Assembly of Metabolite Library for Absolute Quantification
  - LC/MS-Based Metabolomics and Quantification of Metabolite Abundance within Samples
  - Measurement of Whole-Cell Concentrations of Metabolites
  - Rapid Isolation of Mitochondria from Cells and Measurement of Matrix Concentrations of Metabolites
  - Highly Targeted Metabolomics
  - Untargeted Metabolomics
  - Rapid Differential Centrifugation for Isolating Mitochondria
  - Calculations for Matrix Glutamate and Aspartate during RC Dysfunction in the Presence and Absence of Pyruvate
  - Heat Maps
  - Experimental Design
- QUANTIFICATION AND STATISTICAL ANALYSIS
- DATA AND SOFTWARE AVAILABILITY
  - Data Resources

SUPPLEMENTAL INFORMATION

Supplemental Information includes four figures and three tables and can be found with this article online at http://dx.doi.org/10.1016/j.cell.2016.07.040.

AUTHOR CONTRIBUTIONS

W.W.C. and D.M.S. initiated the project and designed the research. E.F. played a critical role in establishing the LC/MS platform, assembling the library of metabolite standards, operating the LC/MS equipment, and performing the absolute quantification of samples. T.W. helped with the generation of the MITObolome and provided computational expertise. K.B. helped with experiments. W.W.C. and D.M.S. wrote and edited the manuscript.

ACKNOWLEDGMENTS

We thank all members of the D.M.S. lab and Hoi See Tsao for helpful suggestions. C4- and C5-carnitines were kindly synthesized by Rajan Pragani and provided by Jared Mayers. This work was supported by grants from the NIH (R01CA103866, R01CA129105, and R37AI047389) and the Department of Defense (W81XWH-15-1-0230 to D.M.S; W81XWH-15-1-0337 to E.F.). Fellowship support was provided by the NIH (F30 AG046047 to W.W.C.; F31 CA189437 to T.W.; K22 CA193660 to K.B.). D.M.S is an investigator of the Howard Hughes Medical Institute.

Received: February 24, 2016
Revised: June 8, 2016
Accepted: July 25, 2016
Published: August 25, 2016

REFERENCES

Berry, M.N., Barritt, G.J., Edwards, A.M., and Burdon, R.H. (1991). Isolated Hepatocytes: Preparation, Properties and Applications: Preparation, Properties and Applications (Elsevier).

Berthet, J., and Baudhuin, P. (1967). A remark about the determination of the water content of mitochondria. J. Cell Biol. *34*, 701–702.

Bestwick, R.K., Moffett, G.L., and Mathews, C.K. (1982). Selective expansion of mitochondrial nucleoside triphosphate pools in antimetabolite-treated HeLa cells. J. Biol. Chem. *257*, 9300–9304.

Birsoy, K., Wang, T., Chen, W.W., Freinkman, E., Abu-Remaileh, M., and Sabatini, D.M. (2015). An essential role of the mitochondrial electron transport chain in cell proliferation is to enable aspartate synthesis. Cell *162*, 540–551.

Bogenhagen, D., and Clayton, D.A. (1974). The number of mitochondrial deoxyribonucleic acid genomes in mouse L and human HeLa cells. Quantitative

isolation of mitochondrial deoxyribonucleic acid. J. Biol. Chem. *249*, 7991–7995.

Bowsher, C.G., and Tobin, A.K. (2001). Compartmentation of metabolism within mitochondria and plastids. J. Exp. Bot. *52*, 513–527.

Cacciatore, S., and Loda, M. (2015). Innovation in metabolomics to improve personalized healthcare. Ann. N Y Acad. Sci. *1346*, 57–62.

Cardaci, S., Zheng, L., MacKay, G., van den Broek, N.J.F., MacKenzie, E.D., Nixon, C., Stevenson, D., Tumanov, S., Bulusu, V., Kamphorst, J.J., et al. (2015). Pyruvate carboxylation enables growth of SDH-deficient cells by supporting aspartate biosynthesis. Nat. Cell Biol. *17*, 1317–1326.

Chantranupong, L., Wolfson, R.L., Orozco, J.M., Saxton, R.A., Scaria, S.M., Bar-Peled, L., Spooner, E., Isasa, M., Gygi, S.P., and Sabatini, D.M. (2014). The Sestrins interact with GATOR2 to negatively regulate the amino-acid-sensing pathway upstream of mTORC1. Cell Rep. *9*, 1–8.

Chen, W.W., Birsoy, K., Mihaylova, M.M., Snitkin, H., Stasinski, I., Yucel, B., Bayraktar, E.C., Carette, J.E., Clish, C.B., Brummelkamp, T.R., et al. (2014). Inhibition of ATPIF1 ameliorates severe mitochondrial respiratory chain dysfunction in mammalian cells. Cell Rep. *7*, 27–34.

Corcelli, A., Saponetti, M.S., Zaccagnino, P., Lopalco, P., Mastrodonato, M., Liquori, G.E., and Lorusso, M. (2010). Mitochondria isolated in nearly isotonic KCl buffer: Focus on cardiolipin and organelle morphology. Biochim. Biophys. Acta *1798*, 681–687.

Elo, J.M., Yadavalli, S.S., Euro, L., Isohanni, P., Götz, A., Carroll, C.J., Valanne, L., Alkuraya, F.S., Uusimaa, J., Paetau, A., et al. (2012). Mitochondrial phenylalanyl-tRNA synthetase mutations underlie fatal infantile Alpers encephalopathy. Hum. Mol. Genet. *21*, 4521–4529.

Erecińska, M., Wilson, D.F., and Nishiki, K. (1978). Homeostatic regulation of cellular energy metabolism: experimental characterization in vivo and fit to a model. Am. J. Physiol. *234*, C82–C89.

Fly, R., Lloyd, J., Krueger, S., Fernie, A., and Merwe, M.J. (2015). Improvements to define mitochondrial metabolomics using nonaqueous fractionation. In Plant Mitochondria: Methods and Protocols, J. Whelan and W.M. Murcha, eds. (Springer), pp. 197–210.

Gerencser, A.A., Chinopoulos, C., Birket, M.J., Jastroch, M., Vitelli, C., Nicholls, D.G., and Brand, M.D. (2012). Quantitative measurement of mitochondrial membrane potential in cultured cells: calcium-induced de- and hyperpolarization of neuronal mitochondria. J. Physiol. *590*, 2845–2871.

Harris, M. (1980). Pyruvate blocks expression of sensitivity to antimycin A and chloramphenicol. Somatic Cell Genet. *6*, 699–708.

Idell-Wenger, J.A., Grotyohann, L.W., and Neely, J.R. (1978). Coenzyme A and carnitine distribution in normal and ischemic hearts. J. Biol. Chem. *253*, 4310–4318.

Kanehisa, M., and Goto, S. (2000). KEGG: kyoto encyclopedia of genes and genomes. Nucleic Acids Res. *28*, 27–30.

Ke, H., Lewis, I.A., Morrisey, J.M., McLean, K.J., Ganesan, S.M., Painter, H.J., Mather, M.W., Jacobs-Lorena, M., Llinás, M., and Vaidya, A.B. (2015). Genetic investigation of tricarboxylic acid metabolism during the *Plasmodium falciparum* life cycle. Cell Rep. *11*, 164–174.

King, M.P., and Attardi, G. (1989). Human cells lacking mtDNA: repopulation with exogenous mitochondria by complementation. Science *246*, 500–503.

Linskens, H.F., Anderson, J.M., Anderson, B., Jackson, J.F., Berkowitz, G.A., Cline, K., Gibbs, M., Goldberg, R., Hirokawa, T., and Huang, A.H.C. (2012). Cell Components (Springer).

Markovitz, P.J., Chuang, D.T., and Cox, R.P. (1984). Familial hyperlysinemias. Purification and characterization of the bifunctional aminoadipic semialdehyde synthase with lysine-ketoglutarate reductase and saccharopine dehydrogenase activities. J. Biol. Chem. *259*, 11643–11646.

Matuszczyk, J.-C., Teleki, A., Pfizenmaier, J., and Takors, R. (2015). Compartment-specific metabolomics for CHO reveals that ATP pools in mitochondria are much lower than in cytosol. Biotechnol. J. *10*, 1639–1650.

Messmer, M., Blais, S.P., Balg, C., Chênevert, R., Grenier, L., Lagüe, P., Sauter, C., Sissler, M., Giegé, R., Lapointe, J., and Florentz, C. (2009). Peculiar inhibition of human mitochondrial aspartyl-tRNA synthetase by adenylate analogs. Biochimie *91*, 596–603.

Mullen, A.R., Wheaton, W.W., Jin, E.S., Chen, P.-H., Sullivan, L.B., Cheng, T., Yang, Y., Linehan, W.M., Chandel, N.S., and DeBerardinis, R.J. (2012). Reductive carboxylation supports growth in tumour cells with defective mitochondria. Nature *481*, 385–388.

Nemoto, Y., and De Camilli, P. (1999). Recruitment of an alternatively spliced form of synaptojanin 2 to mitochondria by the interaction with the PDZ domain of a mitochondrial outer membrane protein. EMBO J. *18*, 2991–3006.

Nishiki, K., Erecińska, M., and Wilson, D.F. (1978). Energy relationships between cytosolic metabolism and mitochondrial respiration in rat heart. Am. J. Physiol. *234*, C73–C81.

Pagliarini, D.J., Calvo, S.E., Chang, B., Sheth, S.A., Vafai, S.B., Ong, S.-E., Walford, G.A., Sugiana, C., Boneh, A., Chen, W.K., et al. (2008). A mitochondrial protein compendium elucidates complex I disease biology. Cell *134*, 112–123.

Palmieri, F. (2013). The mitochondrial transporter family SLC25: identification, properties and physiopathology. Mol. Aspects Med. *34*, 465–484.

Roede, J.R., Park, Y., Li, S., Strobel, F.H., and Jones, D.P. (2012). Detailed mitochondrial phenotyping by high resolution metabolomics. PLoS ONE *7*, e33020.

Ross-Inta, C., Tsai, C.-Y., and Giulivi, C. (2008). The mitochondrial pool of free amino acids reflects the composition of mitochondrial DNA-encoded proteins: indication of a post- translational quality control for protein synthesis. Biosci. Rep. *28*, 239–249.

Safer, B. (1975). The metabolic significance of the malate-aspartate cycle in heart. Circ. Res. *37*, 527–533.

Saldanha, A.J. (2004). Java Treeview–extensible visualization of microarray data. Bioinformatics *20*, 3246–3248.

Scovassi, A.I. (2004). Mitochondrial poly(ADP-ribosylation): from old data to new perspectives. FASEB J. *18*, 1487–1488.

Shaham, O., Slate, N.G., Goldberger, O., Xu, Q., Ramanathan, A., Souza, A.L., Clish, C.B., Sims, K.B., and Mootha, V.K. (2010). A plasma signature of human mitochondrial disease revealed through metabolic profiling of spent media from cultured muscle cells. Proc. Natl. Acad. Sci. USA *107*, 1571–1575.

Srere, P.A., and Sumegi, B. (1986). Organization of the mitochondrial matrix. In Myocardial and Skeletal Muscle Bioenergetics, N. Brautbar and M.A. Boston, eds. (Springer), pp. 13–25.

Stark, R., Pasquel, F., Turcu, A., Pongratz, R.L., Roden, M., Cline, G.W., Shulman, G.I., and Kibbey, R.G. (2009). Phosphoenolpyruvate cycling via mitochondrial phosphoenolpyruvate carboxykinase links anaplerosis and mitochondrial GTP with insulin secretion. J. Biol. Chem. *284*, 26578–26590.

Stark, R., Guebre-Egziabher, F., Zhao, X., Feriod, C., Dong, J., Alves, T.C., Ioja, S., Pongratz, R.L., Bhanot, S., Roden, M., et al. (2014). A role for mitochondrial phosphoenolpyruvate carboxykinase (PEPCK-M) in the regulation of hepatic gluconeogenesis. J. Biol. Chem. *289*, 7257–7263.

Sullivan, L.B., Gui, D.Y., Hosios, A.M., Bush, L.N., Freinkman, E., and Vander Heiden, M.G. (2015). Supporting aspartate biosynthesis is an essential function of respiration in proliferating cells. Cell *162*, 552–563.

Tischler, M.E., Hecht, P., and Williamson, J.R. (1977). Determination of mitochondrial/cytosolic metabolite gradients in isolated rat liver cells by cell disruption. Arch. Biochem. Biophys. *181*, 278–293.

Van Vranken, J.G., and Rutter, J. (2015). You down with ETC? Yeah, you know D!. Cell *162*, 471–473.

Vianey-Liaud, C., Divry, P., Gregersen, N., and Mathieu, M. (1987). The inborn errors of mitochondrial fatty acid oxidation. J. Inherit. Metab. Dis. *10* (*Suppl 1*), 159–200.

Wagner, G.R., and Payne, R.M. (2013). Widespread and enzyme-independent N^{ε}-acetylation and N^{ε}-succinylation of proteins in the chemical conditions of the mitochondrial matrix. J. Biol. Chem. *288*, 29036–29045.

Wallace, D.C. (2013). A mitochondrial bioenergetic etiology of disease. J. Clin. Invest. *123*, 1405–1412.

Wheaton, W.W., Weinberg, S.E., Hamanaka, R.B., Soberanes, S., Sullivan, L.B., Anso, E., Glasauer, A., Dufour, E., Mutlu, G.M., Budigner, G.S., and Chandel, N.S. (2014). Metformin inhibits mitochondrial complex I of cancer cells to reduce tumorigenesis. eLife *3*, e02242.

Wiegand, G., and Remington, S.J. (1986). Citrate synthase: structure, control, and mechanism. Annu. Rev. Biophys. Biophys. Chem. *15*, 97–117.

Williamson, J.R., and Corkey, B.E. (1979). Assay of citric acid cycle intermediates and related compounds—Update with tissue metabolite levels and intracellular distribution. In Methods in Enzymology (Academic Press), pp. 200–222.

Yoshii, S.R., Kishi, C., Ishihara, N., and Mizushima, N. (2011). Parkin mediates proteasome-dependent protein degradation and rupture of the outer mitochondrial membrane. J. Biol. Chem. *286*, 19630–19640.

STAR★METHODS

KEY RESOURCES TABLE

REAGENT or RESOURCE	SOURCE	IDENTIFIER
Antibodies		
Anti-FLAG M2 magnetic beads	Sigma-Aldrich	Cat#M8823
Anti-HA magnetic beads	Thermo Fisher Scientific	Cat#88837
Rabbit monoclonal anti-VDAC	Cell Signaling Technology	Cat#4661; RRID:AB_10557420
Rabbit monoclonal anti-CS	Cell Signaling Technology	Cat#14309
Rabbit monoclonal anti-RPS6KB1	Cell Signaling Technology	Cat#2708; RRID:AB_390722
Rabbit monoclonal anti-GOLGA1	Cell Signaling Technology	Cat#13192
Rabbit monoclonal anti-CALR	Cell Signaling Technology	Cat#12238
Rabbit polyclonal anti-SHMT2	Sigma-Aldrich	Cat#HPA-020549; RRID:AB_1856834
Mouse monoclonal anti-LAMP2	Santa Cruz Biotechnology	Cat#sc-18822; RRID:AB_626858
Rabbit polyclonal anti-LMNA	Santa Cruz Biotechnology	Cat#sc-20680; RRID:AB_648148
Rabbit monoclonal anti-PEX19	Abcam	Cat#ab137072
Chemicals, Peptides, and Recombinant Proteins		
Piericidin A	Enzo Life Sciences	Cat#380-235-M002
Sodium pyruvate solution	Sigma-Aldrich	Cat#S8636
Antimycin A	Sigma-Aldrich	Cat#A8674
Oligomycin A	Sigma-Aldrich	Cat#75351
FCCP	Sigma-Aldrich	Cat#C2920
Verapamil	Sigma-Aldrich	Cat#V4629
MitoTracker Deep Red FM	Thermo Fisher Scientific	Cat#M22426
TMRM	Thermo Fisher Scientific	Cat#T668
Mixture of amino acid standards for metabolomics	Cambridge Isotope Laboratories	Cat#MSK-A2-1.2
Experimental Models: Cell Lines		
Human: HeLa cells	ATCC	CCL-2
Recombinant DNA		
Template plasmid: EGFP-OMP25	Addgene	Plasmid#38249
pMXs-IRES-blasticidin retroviral vector	Cell Biolabs	Cat#RTV-016
Plasmid: 3XFLAG-EGFP-OMP25	This paper	N/A
Plasmid: 3XMyc-EGFP-OMP25	This paper	N/A
Plasmid: 3XHA-EGFP-OMP25	This paper	N/A
Sequence-Based Reagents		
Cloning primer: 3XFLAG_Forward: ATCTCGAGGCCACCATG GACTACAAAGACCATGACGGTGATTATAAAGATCATGACA TTGATTACAAGGATGACGATGACAAGGTGAGCAAGGGCG AGGAGC	This paper	N/A
Cloning primer: 3XMyc_Forward: ATCTCGAGGCCACCATG GAGCAGAAGCTGATTTCTGAGGAAGATCTGGGCACAGG ATCCGAACAGAAACTGATTTCTGAGGAAGATCTGGGCAG CGCCGGAGAGCAGAAGCTGATTTCTGAAGAGGATCTGG GAGGGAGCGGCGTGAGCAAGGGCGAGGAGCTGTTCA CCGGGGTG	This paper	N/A
Cloning primer: 3XHA_Forward: ATCTCGAGGCCACCATG TATCCCTATGACGTGCCTGATTACGCCGGCACAGGATCC TACCCCTATGATGTGCCTGACTACGCTGGCAGCGCCGG ATACCCTTATGATGTGCCTGATTATGCTGGAGGGAGCGG CGTGAGCAAGGGCGAGGAGCTGTTCACCGGGGTG	This paper	N/A

(*Continued on next page*)

Continued

REAGENT or RESOURCE	SOURCE	IDENTIFIER
Cloning primer: OMP25_Reverse: ATGCGGCCGCTCAGA GCTGCTTTCGGTATCTCACGAAG	This paper	N/A
Software and Algorithms		
XCalibur QuanBrowser 2.2	Thermo Fisher Scientific	https://www.thermofisher.com/us/en/home.html
Imaris	Bitplane	http://www.bitplane.com
Progenesis CoMet	Nonlinear Dynamics	http://www.nonlinear.com
Java Treeview	Saldanha, 2004	http://jtreeview.sourceforge.net
R	The R Project for Statistical Computing	https://www.r-project.org
Other		
Homogenizer – plain plunger	VWR International	Cat#89026-398
Homogenizer – 2 ml vessel	VWR International	Cat#89026-386

CONTACT FOR REAGENT AND RESOURCE SHARING

Further information and requests for reagents may be directed to, and will be fulfilled by the corresponding author David M. Sabatini (sabatini@wi.mit.edu). All epitope-tagged constructs can be found on Addgene.

EXPERIMENTAL MODEL AND SUBJECT DETAILS

Generation of Cells with Epitope-Tagged Mitochondria

HeLa cells, an established human cell line, were originally purchased from ATCC. Their identity was confirmed prior to the start of this work through cell line authentication (Duke University DNA Analysis Facility).

Various epitope-tagged constructs were transfected with the retroviral packaging vectors Gag-Pol and CMV VSV-G into HEK293T cells. Media was changed 24 hr after transfection. The virus-containing supernatant was collected 48 hr after transfection and passed through a 0.45 μm filter to eliminate cells. HeLa cells were infected in media containing 8 μg/ml of polybrene and a spin infection was performed by centrifugation at ~1,100 g for 1 hr. Post-infection, virus was removed and cells were selected with blasticidin (10 μg/ml), before being FACS-sorted twice for sufficient EGFP signal.

Cell Culture Conditions

HeLa cells were grown in DME base media containing 10% heat inactivated fetal bovine serum, 4 mM glutamine, penicillin, and streptomycin. For all experiments, cells were cultured in DME base media, DMEM lacking pyruvate (Sigma), or DMEM lacking pyruvate supplemented with 1 mM pyruvate. For each experiment, cells were washed once with PBS before being cultured with the indicated media. For experiments measuring TMRM and TMR, cells were first cultured for 45 min in DME base media with TMRM (25 nM) and verapamil (10 μM), which facilitates loading of TMRM into cells. Cells were then treated with 100% ethanol (1/1000) or FCCP (10 μM) for an additional 30 min before processing. For all other experiments using DME base media, cells were cultured in normal base media for one hr before processing. For experiments comparing the effects of different RC inhibitors, cells were treated for two hr with 100% DMSO (1/1000), piericidin (5 μM), antimycin (10 μM), or oligomycin (5 μM) in DMEM lacking pyruvate. For experiments studying the effects of pyruvate on mitochondrial metabolites during Complex V inhibition, cells were treated for two hr with 100% DMSO (1/1000) or oligomycin (5 μM) in DMEM lacking pyruvate or DMEM lacking pyruvate and supplemented with 1 mM pyruvate.

METHOD DETAILS

Magnetic Beads, Antibodies, Reagents, and Constructs

Materials were obtained from the following sources: Anti-FLAG M2 magnetic beads (M8823) from Sigma-Aldrich; anti-HA magnetic beads (88837) from Thermo Fisher Scientific; antibodies to VDAC (4661), CS (14309), RPS6KB1 (2708), GOLGA1 (13192), and CALR (12238) from Cell Signaling Technology; antibody to SHMT2 (HPA-020549) from Sigma-Aldrich; antibodies to LAMP2 (sc-18822) and LMNA (sc-20680) from Santa Cruz Biotechnology; antibody to PEX19 (ab137072) from Abcam; HRP-conjugated anti-mouse and anti-rabbit antibodies from Santa Cruz Biotechnology; piericidin A from Enzo Life Sciences; sodium pyruvate, polybrene, antimycin A, oligomycin A, FCCP, and verapamil from Sigma-Aldrich; blasticidin from Invivogen; and MitoTracker Deep Red FM and TMRM from Thermo Fisher Scientific.

Retroviral 3XFLAG-EGFP-OMP25, 3XMyc-EGFP-OMP25, 3XHA-EGFP-OMP25 vectors were generated via ligation of fragments PCR-amplified from an EGFP-OMP25 construct (Addgene, #38249) (Yoshii et al., 2011) into a pMXs-IRES-blasticidin retroviral vector (Cell Biolabs) digested with XhoI and NotI.

Immunoblotting

Protein from lysates were prepared for and resolved by 12% SDS-PAGE at 100 V, transferred for 2.5 hr at 50 V onto 0.45 μm PVDF membranes, and analyzed by immunoblotting as described previously (Chantranupong et al., 2014). Membranes were blocked with 5% nonfat dry milk prepared in TBST (tris-buffered saline with Tween 20) for 45 min at room temperature, then incubated with primary antibodies in 5% milk overnight at 4°C. Primary antibodies to the following proteins were used at the indicated dilutions: VDAC (1/1000), CS (1/1000), RPS6KB1 (1/1000), GOLGA1 (1/1000), CALR (1/1000), SHMT2 (1/1000), LAMP2 (1/2000), LMNA (1/1000), and PEX19 (1/1000). Membranes were then washed three times, 5 min each, with TBST and incubated with the corresponding secondary antibodies in 5% milk (1/5000) for 45 min at room temperature. Membranes were then washed three more times, 5 min each, with TBST before being visualized using enhanced chemiluminescence (Thermo Fisher Scientific).

Confocal Microscopy

For experiments confirming proper localization of the epitope-tagged protein to mitochondria, ~60,000 HeLa cells expressing different 3XTag-EGFP-OMP25 constructs were incubated with 6.25 nM - 25 nM MitoTracker Deep Red FM (MTDR) (Thermo Fisher Scientific) for one hr. Cells were then fixed with 4% PFA in PBS, mounted with anti-fade mounting medium containing DAPI (Vectashield), and imaged on an RPI spinning disk confocal microscope (Zeiss) using EGFP, MTDR, and DAPI channels. For imaging mitochondria on beads, 4% PFA in PBS was used instead of 80% methanol during the mitochondrial IP workflow (see below). Images of mitochondria were acquired as described for whole cells, except that the DAPI channel was not used.

MITObolome and Assembly of Metabolite Library for Absolute Quantification

The high-confidence list of 1,023 human mitochondrial proteins from MitoCarta (Pagliarini et al., 2008) was cross-referenced with a list of 2,990 known metabolic enzymes and transporters (Birsoy et al., 2015) to give a set of 479 mitochondrial enzymes and transporters. For these 479 proteins, KEGG (Kanehisa and Goto, 2000) and manual curation were used to identify their cognate substrates, products, and cofactors, which formed a draft list of predicted mitochondrial metabolites. Metabolites not listed in KEGG but involved in critical mitochondrial processes were added to the draft list as well (e.g., certain proteinogenic amino acids are not acted upon by any known enzyme or transporter but are needed for mRNA translation in mitochondria). Finally, certain molecules were removed because they are not actually metabolites (e.g., carrier proteins conjugated to small molecules). Additional modifications, such as removal of metals and non-endogenous compounds, were also made to generate the final list of 346 metabolites predicted to be present in human mitochondria, which was termed the "MITObolome" (see Table S1 for complete list of the added/removed metabolites). Using the MITObolome, a library of 132 metabolites was assembled to generate standard curves for absolute quantification of samples (see Table S1 for complete details).

LC/MS-Based Metabolomics and Quantification of Metabolite Abundance within Samples

LC/MS was used to profile and quantify the polar metabolite contents of both whole-cell and IP samples. Acetonitrile was Hypergrade and was purchased from EMD Millipore. All other solvents were Optima LC/MS grade and were purchased from Thermo Fisher Scientific. The metabolite extraction mix was composed of 80% methanol in water, supplemented with a mixture of 17 isotope-labeled amino acids at 90.9 nM each, which were used as internal standards (Cambridge Isotope Laboratories, MSK-A2-1.2).

A library of metabolite chemical standards was curated as described above. Metabolites were commercially available and grouped into five pools (see Table S1 for the composition of each pool), except that C4- and C5-carnitines were a kind gift of R. Pragani and M. Boxer (NCATS, NIH, Rockville, MD) and were synthesized via a published procedure (Goel, Om P., SSV Therapeutics, Inc., USA; U.S. Patent Number 7777071, B2; Aug. 17, 2010). Standards were validated by using LC/MS to confirm that they contained a robust peak at the correct m/z ratio. Stock solutions of each pool, containing 1 mM of each metabolite standard in water, were stored at −80°C. On the day of each LC/MS run, these 1 mM stocks were used to prepare fresh standard curves diluted with 80% methanol in water containing the 17 isotope-labeled internal standards. These standard curves of metabolites within the five pools were then analyzed in parallel with each batch of biological samples.

LC/MS-based analyses were performed as described previously (Birsoy et al., 2015) on a QExactive benchtop orbitrap mass spectrometer equipped with an Ion Max source and a HESI II probe, which was coupled to a Dionex UltiMate 3000 UPLC system (Thermo Fisher Scientific). External mass calibration was performed using the standard calibration mixture every 7 days. 5 μl of each metabolite sample was injected onto a ZIC-pHILIC 2.1 × 150 mm (5 μm particle size) column (EMD Millipore). Buffer A was 20 mM ammonium carbonate, 0.1% ammonium hydroxide; buffer B was acetonitrile. The chromatographic gradient was run at a flow rate of 0.150 ml/min as follows: 0–20 min: linear gradient from 80% to 20% B; 20–20.5 min: linear gradient from 20% to 80% B; 20.5–28 min: hold at 80% B. The mass spectrometer was operated in full-scan, polarity switching mode with the spray voltage set to 3.0 kV, the heated capillary held at 275°C, and the HESI probe held at 350°C. The sheath gas flow was set to 40 units, the auxiliary gas flow was set to 15 units, and the sweep gas flow was set to 1 unit. The MS data acquisition was performed in a range of 70–1000 m/z, with the resolution set at 70,000, the AGC target at 10^6, and the maximum injection time at 80 ms.

Metabolite identification and quantification were performed with XCalibur QuanBrowser 2.2 (Thermo Fisher Scientific) using a 10 ppm mass accuracy window and 0.5 min retention time window. To confirm metabolite identities and to enable quantification, the aforementioned pools of authentic metabolite standards were used. Within-batch mass deviation was typically < 0.0005 Da, and retention time deviation was < 0.25 min. Typically, the final concentrations of standards were 1 nM, 10 nM, 100 nM, 1 μM, 10 μM, and 30 μM, but pool 4 was run at concentrations of 1 nM, 3 nM, 10 nM, 30 nM, 100 nM, 300 nM, 1 μM, 3 μM, 10 μM, and 30 μM to more accurately quantify certain metabolites. In each sample, the raw peak area for each metabolite was divided by the raw peak area of the relevant isotope-labeled internal standard to calculate the relative abundance (see Table S1 for the internal standard used for each metabolite). Leucine, isoleucine, methionine, proline, tyrosine, threonine, histidine, aspartate, glutamate, arginine, phenylalanine, and valine were normalized with their isotope-labeled counterparts. All other isotope-labeled amino acids were not abundant enough to give robust peaks in every biological sample and were thus not used. For determining the relative abundances of all other metabolites, the peak areas were normalized to either isotope-labeled phenylalanine or isotope-labeled valine, depending on which isotope-labeled standard had the closer retention time to the metabolite being examined. The relative abundances obtained from the standard curve samples were fit to a quadratic log-log equation, typically with $r^2 > 0.99$, which was then used to calculate the concentration of the metabolite in each metabolite extract. The total number of moles of a metabolite in a given whole-cell or IP extract was then calculated from the sample concentration and the corresponding sample volume. For undetectable metabolites, concentrations were set to 0.

LC/MS matrix effects (i.e., the effects of KPBS on the behavior of metabolites) were controlled for by comparing the performance of all 132 metabolites in the quantitative profiling library in the presence and absence of KPBS. To model the residual wet volume left over after the IP, a surrogate matrix composition of 2 μl of KPBS for every 48 μl of 80% methanol extraction buffer was used (1/25 dilution). Standard curves were generated using either normal 80% methanol/20% water with internal standards (80/20) or 80% methanol/20% water with internal standards and with KPBS spiked in at a 1/25 dilution (80/20K). Importantly, KPBS did not affect our ability to confidently assign a peak to a particular metabolite, as KPBS did not alter the retention time of the metabolites that were examined. The standard curves derived from 80/20 samples were then used to calculate the concentrations of the 80/20 and 80/20K samples to determine how much deviation there was between the two. Based on the median deviation across multiple concentrations of standards prepared in 80/20 or 80/20K, a list of correction factors was generated for adjusting the quantification of each metabolite within a given IP extract (see Table S1 for correction factors).

Measurement of Whole-Cell Concentrations of Metabolites

All whole-cell metabolite profiling was performed on ice or at 4°C with pre-chilled buffers. Following the appropriate treatment, ~2 million HeLa cells expressing HA-MITO were quickly washed twice with PBS prepared in Optima LC/MS water and then scraped into 500 μl of 80% methanol in water containing the 17 isotope-labeled internal standards. Samples were vortexed vigorously for 10 min, spun down at 17,000 x *g* for 10 min, and the supernatants analyzed with LC/MS as described above to determine the total moles of a metabolite in each whole-cell sample.

For each experiment, a replicate set of cells was treated identically and used for measuring cell number and volume. The contents of each well were trypsinized and cell number and volume measured using a Beckman Z2 Coulter Counter with a size setting of 8-30 μm.

Whole-cell concentrations were calculated using the total moles of a metabolite in a whole-cell sample, the total number of cells per sample, and the volume of each cell.

Rapid Isolation of Mitochondria from Cells and Measurement of Matrix Concentrations of Metabolites

Traditional mitochondrial isolation buffer was made of 75 mM sucrose, 225 mM mannitol, 20 mM HEPES, 0.5 mM EDTA, pH 7.4, cOmplete EDTA-free protease inhibitor (Roche) in deionized water. LC/MS-compatible mitochondrial isolation buffer, KPBS, was comprised of 136 mM KCl, 10 mM KH_2PO_4, pH 7.25 in Optima LC/MS water and was prepared using clean equipment and glassware. The pH of the buffer was adjusted with KOH because of the sensitivity of isolated mitochondria to sodium. After passage through a 0.22 μm filter (Corning), the buffer was kept at 4°C.

For each experiment, an anti-HA IP was performed on HeLa cells expressing Control-MITO or HA-MITO. The entire workflow was done on ice in a 4°C cold room with pre-chilled buffers and equipment. Only one sample (i.e., Control-MITO or HA-MITO-expressing cells) was processed at a time to increase the speed of isolation. 200 μl of anti-HA magnetic beads were pre-washed three times with KPBS. All washes were done by gentle pipetting using a wide-bore pipette tip and collecting beads using a DynaMag Spin Magnet (Thermo Fisher Scientific).

~30 million cells were rapidly washed twice with PBS prepared in Optima LC/MS water and then gently scraped into 1 ml KPBS. The cell suspension was spun down at 1000 x *g* for 2 min, supernatant was discarded, and cell pellet gently resuspended in 1 ml KPBS. Cells were homogenized with 25 strokes of a 2 ml homogenizer containing a pure PTFE head (VWR International), taking care not to introduce air bubbles into the solution. The homogenate was spun down at 1000 x *g* for 2 min and the supernatant incubated with 200 μl of prewashed beads on an end-over-end rotator for 3.5 min. Afterward, the IP was quickly washed twice with 1 ml KPBS, resuspended in 1 ml KPBS, and transferred to a new tube. 250 μl of the suspension was taken for detergent lysis and the remainder for metabolite extraction. Metabolites were always extracted before detergent lysis. For metabolite extraction, beads were collected and incubated for 5 min with 50 μl of 80% methanol in water containing internal standards. For detergent lysis, beads

were collected and incubated for 10 min with 50 μl of lysis buffer comprised of 50 mM Tris-HCl, pH 7.4, 150 mM NaCl, 1 mM EDTA, 1% Triton X-100, and cOmplete EDTA-free protease inhibitor. Afterward, the detergent lysate and metabolite extract were transferred to new tubes, spun down at 17,000 x *g* for 10 min, and the supernatants kept.

In experiments examining the effects of a lengthened workflow on matrix metabolite profiles, all steps were identical except that IP samples sat on ice for an additional 4 min before the final wash solution was aspirated and samples were processed further.

The metabolite extract was analyzed with LC/MS as described earlier to determine the total moles of a metabolite in each IP sample. For a metabolite to be considered present at levels above background (i.e., to be considered mitochondrial), it had to be at least 1.5-fold more abundant in the HA-MITO IP than in the Control-MITO IP across three biological replicates. The background-corrected abundance was obtained by subtracting the moles present in the Control-MITO IP from those present in the HA-MITO IP.

To determine the corresponding matrix volume for a given HA-MITO IP, a two-part strategy was used. First, ~60,000 HA-MITO-expressing cells were cultured under the same conditions used for all metabolite profiling experiments, and then fixed, mounted, and imaged using the EGFP and DAPI channels. Z-stacks of at least 100 cells per condition were generated using a step size of 0.25 μm. The three-dimensional surface of the EGFP signal (surface area detail = 0.05 μm, diameter of largest sphere that will fit into object = 0.25 μm) was created with the IMARIS software (Bitplane) and the total mitochondrial volume per cell calculated with the built-in volumetric analysis. The mean mitochondrial volume per cell in each condition was used for subsequent calculations.

For the second part of our approach, a defined number of HA-MITO-expressing cells were lysed as described above. A series of dilutions of this cell lysate was analyzed in parallel with HA-MITO IP samples by blotting for citrate synthase, a protein that is predominantly localized to the mitochondria within cells (Wiegand and Remington, 1986). Using densitometry analysis, the total number of whole-cell equivalents present in each HA-MITO IP could be determined. The dilution series behaved linearly with r^2 ~0.97.

The final matrix volume associated with each HA-MITO IP was then calculated using the total mitochondrial volume per cell, the number of whole-cell equivalents present in each HA-MITO IP, and the proportion of mitochondrial volume occupied by an orthodox configuration of the matrix (~63.16% of mitochondrial volume = matrix) (Gerencser et al., 2012). Matrix concentrations of metabolites were determined by combining the background-corrected moles of a metabolite in the HA-MITO IP with the corresponding matrix volume.

Highly Targeted Metabolomics

For the highly targeted analyses of TMRM and TMR and certain nucleotide species, the instrument was run as described above, but with the following modifications. For TMRM and TMR, an additional tSIM (targeted selected ion monitoring) scan in positive ionization mode was done, with the resolution set to 70,000, an AGC target of 10^5, and a maximum integration time of 250 ms. The target masses were 401.1860 (corresponding to TMRM) and 387.1703 (corresponding to de-esterified TMRM, i.e., TMR). The isolation window around each target mass was set to 1.0 m/z. Only relative quantification was done for TMRM and TMR. For the nucleotide analysis, MS data was collected in negative ionization mode only, in a mass range of 285-550 m/z, with the resolution set to 70,000, an AGC target of 10^6, and a maximum integration time of 250 ms.

Untargeted Metabolomics

Positive and negative ionization data from LC/MS-based analysis of control and HA-MITO IP samples was interrogated with Progenesis CoMet software (Nonlinear Dynamics). See Table S1 for complete list of criteria used to determine if a metabolite was present at levels above background (i.e., if a metabolite was mitochondrial).

Rapid Differential Centrifugation for Isolating Mitochondria

For experiments isolating mitochondria using rapid differential centrifugation, a modified workflow based on existing protocols was used (Bestwick et al., 1982; Bogenhagen and Clayton, 1974). All experiments were performed using KPBS to make the isolation conditions of the differential centrifugation consistent with those of the IP method. All steps of the centrifugation workflow leading up to the post-homogenization spin were identical to those of the IP method described above. The homogenate was spun down at 1000 x *g* for 2 min and the supernatant taken and spun down at 10,000 x *g* for 10 min. After aspirating the supernatant, the pellet was washed with 1 ml of KPBS by gentle resuspension, and then transferred to a new tube. The suspension was spun again at 10,000 x *g* for 10 min, after which the supernatant was aspirated and the pellet was incubated with 100 μl lysis buffer (see above) for 10 min on ice. Afterward, the detergent lysate was transferred to a new tube, spun down at 17,000 x *g* for 10 min, and the supernatant kept. For experiments comparing the specificity of differential centrifugation to the IP method, 100 μl of lysis buffer was also used to lyse mitochondria isolated by the anti-HA beads.

Calculations for Matrix Glutamate and Aspartate during RC Dysfunction in the Presence and Absence of Pyruvate

Matrix concentrations from Table S3 were used for all calculations. To streamline the explanation of the calculations, the following abbreviations will be used: V = vehicle-treated; O = oligomycin-treated; VP = vehicle-treated, pyruvate-supplemented; OP = oligomycin-treated, pyruvate-supplemented. To calculate the pyruvate-driven changes in matrix aspartate during RC dysfunction, the following steps were done. Because the concentration of matrix aspartate in VP cells was significantly lower than that of V cells ($p < 0.05$, $n = 3$), the expected matrix concentration of aspartate in OP cells was first calculated by multiplying each replicate of matrix aspartate concentrations from VP cells by 0.3014, the average fractional abundance of matrix aspartate in O cells relative to V cells.

The resulting triplicate set of expected matrix concentrations of aspartate in OP cells was significantly different from the measured matrix concentrations of aspartate in OP cells ($p < 0.05$, $n = 3$). As such, the average expected matrix concentration of aspartate (141.85 μM) was subtracted from each replicate of the measured matrix concentrations of aspartate in OP cells to obtain a triplicate set of changes in matrix aspartate upon pyruvate supplementation during RC dysfunction.

To calculate the pyruvate-driven changes in matrix glutamate during RC dysfunction, the following steps were done. The matrix concentrations of glutamate in V and VP cells were not significantly different, so it was unnecessary to calculate an expected matrix concentration of glutamate for OP cells. Because the matrix glutamate concentrations of O and OP cells were significantly different ($p < 0.05$, $n = 3$), the average matrix glutamate concentration of O cells was subtracted from each replicate of the matrix glutamate concentrations of OP cells to give a triplicate set of changes in matrix glutamate upon pyruvate supplementation during RC dysfunction.

Heat Maps

Heat maps were generated using Java TreeView (Saldanha, 2004). See Tables S2 and S3 for complete lists of criteria used to assemble heat maps.

Experimental Design

Experiments were not done in a blinded fashion. All instances where n replicates are reported had n biological replicates.

QUANTIFICATION AND STATISTICAL ANALYSIS

P-values in the Table S1 panels, "Untargeted pos-measurements" and "Untargeted neg-measurements," were calculated using an unpaired, one-tailed, heteroscedastic student's *t* test in Microsoft Excel. All other p values were calculated using an unpaired, two-tailed, parametric student's *t* test in GraphPad Prism 6, except for the Table S3 panel "Pyruvate's effects – stat. sig.," for which an identical t test was performed but in Microsoft Excel rather than GraphPad Prism 6. All r^2 values were derived from Pearson correlation coefficients calculated in either GraphPad Prism 6 or Microsoft Excel. Principal components analysis (Figure 3) and a Pearson correlation analysis of fold-changes in metabolite abundance (Figure 5) were performed and visualized using R. The exact value of n, the definition of center and precision measures, and p values are provided in all figure legends. The exact values of n and p values for data analyses can also be found in Tables S1 and S3 and certain portions of the STAR Methods. All instances where n replicates are reported had n biological replicates.

Measurements of urate are not included in Table S2 "Whole-cell, piericidin" and Table S2 "Matrix, piericidin" because $r^2 < 0.99$ for the standard curve. Measurements of lactate in IP samples are not included in Tables S1, S2, and S3 because of the low abundance and resulting poor peak quality of lactate in those samples. These exclusions are also detailed in the relevant panels of Tables S1, S2, and S3.

DATA AND SOFTWARE AVAILABILITY

Data Resources

Datasets can be found in Tables S1, S2, and S3.

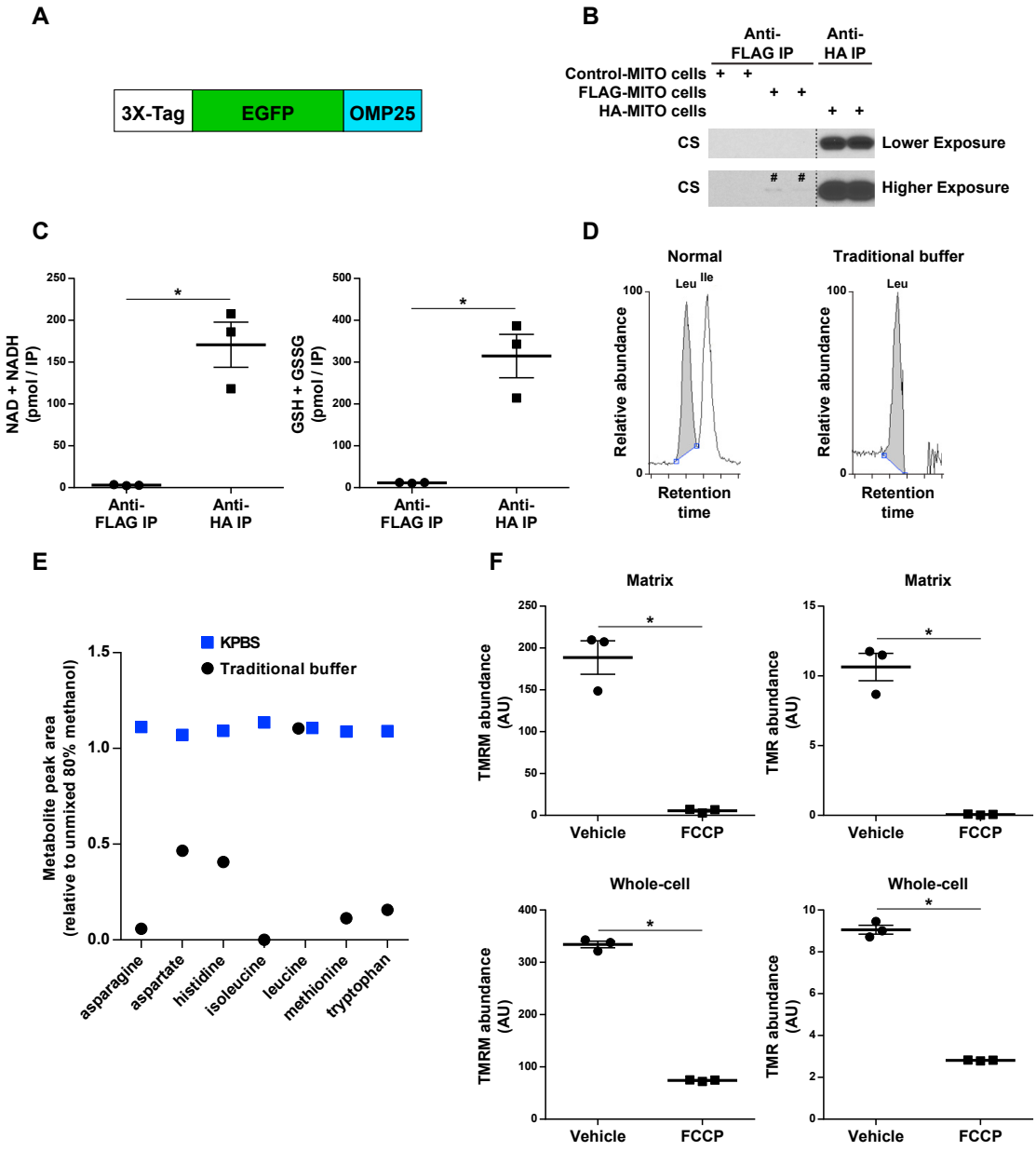

Figure S1. Optimization of Immunocapture and LC/MS Compatibility for Metabolite Profiling of Mitochondria, Related to Figure 1

(A) Schematic depicting general design of epitope-tagged protein. OMP25 represents the amino acid sequence localizing the recombinant protein to the outer mitochondrial membrane.

(B) Anti-HA beads capture more mitochondria than anti-FLAG beads do based on protein markers. Equal volumes of packed beads and identical workflows were used for all experiments. Cells expressing 3XMyc-EGFP-OMP25 (Control-MITO cells), 3XFLAG-EGFP-OMP25 (FLAG-MITO cells), and 3XHA-EGFP-OMP25 (HA-MITO cells) were cultured in DME base media. # signs highlight the presence of faint bands. Similar to the anti-FLAG IP, the amount of mitochondria present in an anti-HA IP of cells expressing 3XMyc-EGFP-OMP25 is undetectable, as shown in Figure 1D using CS, as well as VDAC and SHMT2 as protein markers.

(C) Anti-HA beads capture more mitochondria than anti-FLAG beads do based on metabolite markers. Cells were cultured in DME base media. All measurements are presented as total moles of metabolites present in each IP after subtracting the background values present in the corresponding control IP (mean ± SEM, n = 3, *$p < 0.05$).

(D) Components of traditional isolation buffers can distort metabolite profiles. Representative extracted ion chromatograms are shown for m/z = 132.1019 ± 5 ppm, corresponding to leucine (gray, Leu) and isoleucine (white, Ile). Normal, 80% methanol with 1 μM each of leucine and isoleucine; Traditional buffer, 1:1 mixture of traditional isolation buffer and 80% methanol with leucine and isoleucine.

(E) KPBS performs significantly better than traditional isolation buffers in LC/MS-based analyses. 80% methanol containing the indicated amino acids at 1 μM each was mixed 1:1 with traditional isolation buffer (black) or KPBS (blue). Metabolite peak areas within each sample were first divided by the corresponding values present in unmixed 80% methanol containing the indicated amino acids. To adjust for the effects of diluting the 80% methanol with the different buffers,

(legend continued on next page)

each metabolite was then also normalized with isotope-labeled phenylalanine, which was present at a concentration of 90.9 nM in the 80% methanol and was unaffected by the choice of buffer.

(F) Isolated mitochondria retain a membrane-potential responsive pool of TMRM and TMR. Cells were cultured in DME base media and treated with TMRM (25 nM) for 45 min before being given vehicle (ethanol) or FCCP (10 μM) for 30 min. For a given graph, relative quantification of TMRM and TMR abundance in whole cells or the mitochondrial matrix was performed and samples were normalized based on the amount of cells or mitochondrial material present at the time of extraction, respectively (mean ± SEM, n = 3, *$p < 0.05$).

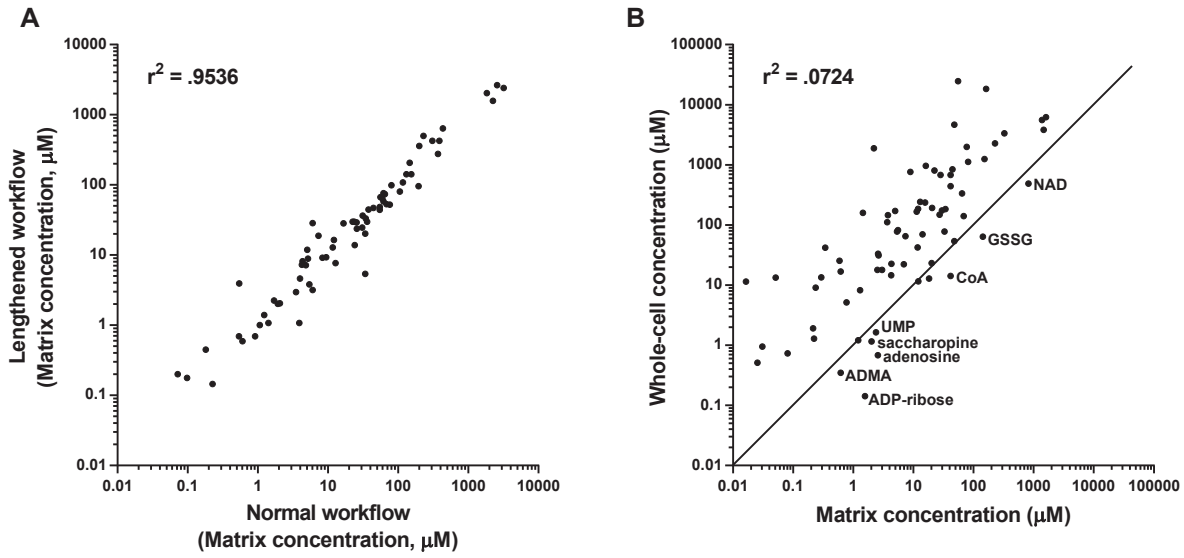

Figure S2. Global Analyses of Mitochondrial Matrix Profiles, Related to Figure 2

(A) Slightly lengthening the IP workflow does not cause a large distortion of the metabolite profile. The lengthened workflow was 4 min longer than the normal workflow.

(B) Comparison of whole-cell versus matrix concentrations. A line is drawn at y = x to indicate where whole-cell and matrix concentrations are equal. Select metabolites that are more concentrated in the matrix than in whole cells are highlighted. For all panels, cells were cultured in DME base media, the means of biological triplicates are shown, and a Pearson correlation coefficient was calculated.

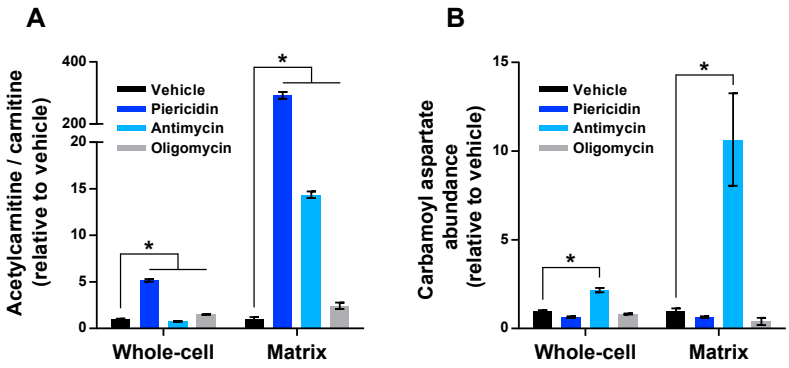

Figure S3. Changes in Mitochondrial Metabolites Specific to Inhibition of Complexes I and III, Related to Figure 4

(A) Complex I inhibition substantially increases the matrix acetylcarnitine/carnitine ratio.

(B) Inhibition of Complex III increases carbamoyl aspartate. For all panels, experiments were performed in DMEM without pyruvate and all measurements are normalized to the corresponding whole-cell or matrix concentrations of vehicle-treated cells (mean ± SEM, n = 3, *p < 0.05).

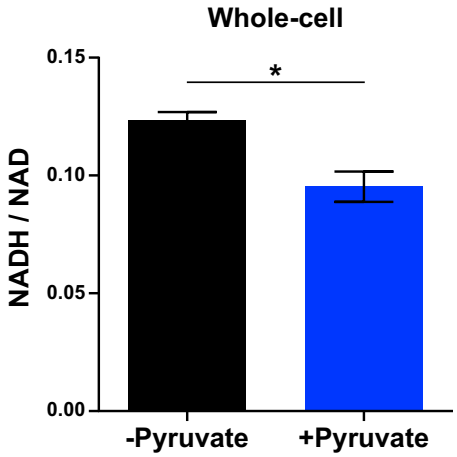

Figure S4. Pyruvate Drives NAD Regeneration, Related to Figure 5

Pyruvate supplementation decreases the whole-cell NADH/NAD ratio. Data are presented as whole-cell NADH/NAD ratios that have not been normalized. Because there was no significant increase in the NADH/NAD ratio upon oligomycin treatment, NADH/NAD ratios from cells treated with either vehicle or oligomycin were averaged for each media condition. Experiments were performed in DMEM with and without pyruvate (1 mM) and measurements are presented as the mean ± SEM, n = 6, *$p < 0.05$.